1998-09

Quantitative structural reliability assurance through finite element analysis

Rice, Christopher W.

Monterey, California: Naval Postgraduate School

NAVAL POSTGRADUATE SCHOOL
Monterey, California

THESIS

QUANTITATIVE STRUCTURAL RELIABILITY ASSURANCE THROUGH FINITE ELEMENT ANALYSIS

by

Christopher W. Rice

September 1998

Thesis Advisor: Edward M. Wu

Approved for public release; distribution is unlimited.

REPORT DOCUMENTATION PAGE

Form Approved
OMB No. 0704-0188

1. AGENCY USE ONLY *(Leave blank)*	2. REPORT DATE	3. REPORT TYPE AND DATES COVERED
	September 1998	Engineer's Thesis

4. TITLE AND SUBTITLE
QUANTITATIVE STRUCTURAL RELIABILITY ASSURANCE THROUGH FINITE ELEMENT ANALYSIS

5. FUNDING NUMBERS
Contract Number
N0042198WR 14350
Amendment 1

6. AUTHOR(S)
Rice, Christopher W.

7. PERFORMING ORGANIZATION NAME(S) AND ADDRESS(ES)
Naval Postgraduate School
Monterey, CA 93943-5000

8. PERFORMING ORGANIZATION REPORT NUMBER

9. SPONSORING / MONITORING AGENCY NAME(S) AND ADDRESS(ES)
Commander, Naval Air Systems Command (PMA-290)
Bldg. 2272, 47123 Buse Rd., Patuxent River, MD 20670

10. SPONSORING/MONITORING AGENCY REPORT NUMBER

11. SUPPLEMENTARY NOTES
The views expressed in this thesis are those of the author and do not reflect the official policy or position of the Department of Defense or the U.S. Government.

12a. DISTRIBUTION / AVAILABILITY STATEMENT
Approved for public release; distribution unlimited.

12b. DISTRIBUTION CODE

13. ABSTRACT ***(Maximum 200 words)***

Risk assessment of aging aircraft components can be achieved by operational de-rating using a safety factor subjectively selected from experience and heuristics. This investigation involves synthesizing currently available, maturing computer-aided methods into a format of objective quantitative risk assessment. The methodology is applied to quantify the effect of corrosion on P-3C main landing gear lower drag struts. This kind of synthesis is appropriate wherever structural operational risk is a concern. The P-3 has undergone many modifications since the 1950s and the lower drag struts are being scrapped due to internal surface corrosion. The corrosion process is random, resulting in pits varied spatially and in severity. These corrosion attributes are merged into a one random variable probability model. The casual relation of the corrosion to structural load is analyzed by finite elements. The structural configuration model input is provided by computer-aided drafting, verified by physical measurement. The effect of corrosion on current strut population reliability, as well as the future, is computed. The conclusion is that even under severe corrosion, compressive buckling is not an issue. All the other failure modes (compressive yielding, tensile yielding, and fracture by fatigue) can be assured by one cold temperature proof test.

14. SUBJECT TERMS
Column Buckling, Corrosion, Finite Element Analysis, Probability, Reliability Assurance, Risk Assessment

15. NUMBER OF PAGES
95

16. PRICE CODE

17. SECURITY CLASSIFICATION OF REPORT	18. SECURITY CLASSIFICATION OF THIS PAGE	19. SECURITY CLASSIFICATION OF ABSTRACT	20. LIMITATION OF ABSTRACT
Unclassified	Unclassified	Unclassified	UL

Approved for public release; distribution is unlimited

QUANTITATIVE STRUCTURAL RELIABILITY ASSURANCE THROUGH FINITE ELEMENT ANALYSIS

Christopher W. Rice
Commander (Select), United States Navy
B.S., United States Naval Academy, 1983
M.S., Naval Postgraduate School, 1998

Submitted in partial fulfillment of the
requirements for the degree of

AERONAUTICAL AND ASTRONAUTICAL ENGINEER

from the

NAVAL POSTGRADUATE SCHOOL
September 1998

Author: [redacted]
Christopher W. Rice

Approved by: [redacted]
Edward M. Wu, Thesis Advisor

[redacted]
Gerald H. Lindsey, Second Reader

[redacted]
Gerald H. Lindsey, Chairman
Department of Aeronautics and Astronautics

ABSTRACT

Risk assessment of aging aircraft components can be achieved by operational de-rating using a safety factor subjectively selected from experience and heuristics. This investigation involves synthesizing currently available, maturing computer-aided methods into a format of objective quantitative risk assessment. The methodology is applied to quantify the effect of corrosion on P-3C main landing gear lower drag struts. This kind of synthesis is appropriate wherever structural operational risk is a concern. The P-3 has undergone many modifications since the 1950's and the lower drag struts are being scrapped due to internal surface corrosion. The corrosion process is random, resulting in pits varied spatially and in severity. These corrosion attributes are merged into a one random variable probability model. The casual relation of the corrosion to structural load is analyzed by finite elements. The structural configuration model input is provided by computer-aided drafting, verified by physical measurement. The effect of corrosion on current strut population reliability, as well as the future, is computed. The conclusion is that even under severe corrosion, compressive buckling is not an issue. All the other failure modes (compressive yielding, tensile yielding, and fracture by fatigue) can be assured by one cold temperature proof test.

TABLE OF CONTENTS

I. INTRODUCTION 1

A. BACKGROUND 1
B. LANDING GEAR DRAG STRUT 2
C. LOADING 3
D. FAILURE MODES 4
E. INTERNAL CORROSION 4
F. CORROSION CHARACTERIZATION 5
G. CURRENT INSPECTION TECHNIQUES 7
H. ANALYSIS METHODOLOGY 7

II. PROBABILISTIC RELIABILITY 9

A. CONTINUOUS RANDOM VARIABLES 9
B. PROBABILITY DISTRIBUTIONS 9
C. DISCRETE RANDOM VARIABLES 10
D. SPECIFIC DISCRETIZED RANDOM VARIABLES 10
E. PIT SEVERITY PROBABILITY DISTRIBUTION 15
F. RANDOM VARIABLE REALIZATION BY FINITE ELEMENTS 19

III. APPLICATION OF FINITE ELEMENTS 21

A. ASSURANCE OF COMPUTATIONAL RESULTS 21
B. LINEAR ELASTIC BUCKLING 22
C. EIGENVALUE DECOMPOSITION 23
D. CONVERGENCE OF ANALYSIS RESULTS 23
E. MIDSIDE NODES AND CONVERGENCE 24
F. THREE DIMENSIONAL ELEMENTS 25
G. ASSUMPTION OF CONSISTENT CONVERGENCE 26

IV. MODELING 27

A. MODELING BY GEOMETRY 27
B. MODELING BY FINITE ELEMENTS 27
C. MODEL VALIDATION THROUGH MASS PROPERTIES 29
D. MODELING OF EQUIVALENT SPHERICAL PITS 29

V. DRAG STRUT BUCKLING ANALYSIS RESULTS 31

A. NOMINAL CASE 31
B. SIX MOST SEVERE PITS 33
C. COMPLETELY THIN SECTION 34
D. MORE SEVERE SPHERICAL PITS 35
E. HOLES AT NODE 1 36
F. HOLES AT NODE 2 38

G. COMBINATIONS OF HOLES AT NODES 1 & 2 39
H. OTHER HOLE COMBINATIONS 39
I. BUCKLING ANALYSIS SUMMARY 41

VI. RISK ASSESSMENT FROM A SINGLE RANDOM VARIABLE 43

A. COLUMN BUCKLING RISK ASSESSMENT 43
B. YIELD AND FRACTURE RISK ASSESSMENT 45
C. COMBINED RISK ASSESSMENT 47

VII. CONCLUSIONS 49

VIII. RECOMMENDATIONS 51

LIST OF REFERENCES 53

APPENDIX A. REJECTED DRAG STRUT PROCESSING 55

APPENDIX B. EQUIVALENT SPHERICAL PIT JUSTIFICATION 67

APPENDIX C. DRAG STRUT MODELING PROCEDURE 69

APPENDIX D. ALUMINUM TUBE BUCKLING TESTS 79

INITIAL DISTRIBUTION LIST 83

ACKNOWLEDGEMENT

The author would like to acknowledge the financial support of the P-3C Class Desk Officer, Program Manager Air, Maritime Surveillance Aircraft (PMA-290), for allowing the purchase of software and equipment used in this thesis. This work was performed under Contract N0042198WR 14350/SRP.

I wish to thank my thesis advisor, Professor Ed Wu, for his incredible dedication to his work and the students that are fortunate enough to be in his company. I am forever indebted to him for his inspiration and guidance, both in this research, and life in general.

I am especially thankful for my wife Beth and our children Adam and Margaret, for their support, understanding, and patience during the long days of this project. Perhaps now I can return to a normal state of mind and not be constantly preoccupied.

Finally, I must acknowledge my Lord and Savior, Jesus Christ. He is my strength and final justification for my life. Through prayer and petition I have been able to complete this work. Amen.

I. INTRODUCTION

A. BACKGROUND

The P-3C "Orion" is a four engine, low-wing aircraft designed for patrol and antisubmarine warfare operated by the U.S. Navy and several other countries. The aircraft was originally designed and built by the Lockheed Aircraft Corporation in Burbank, California beginning in the late 1950s. It has undergone several upgrades and modifications, including clearance to operate at heavyweight loading conditions in 1966. Figure I-1 shows a P-3C in flight with a full load of armament. The landing gear are in a tricycle arrangement with two main gear and one nose gear. All three landing gear incorporate hollow cylinder components that are open to the environment and have experienced varying degrees of internal surface corrosion after many years of fleet

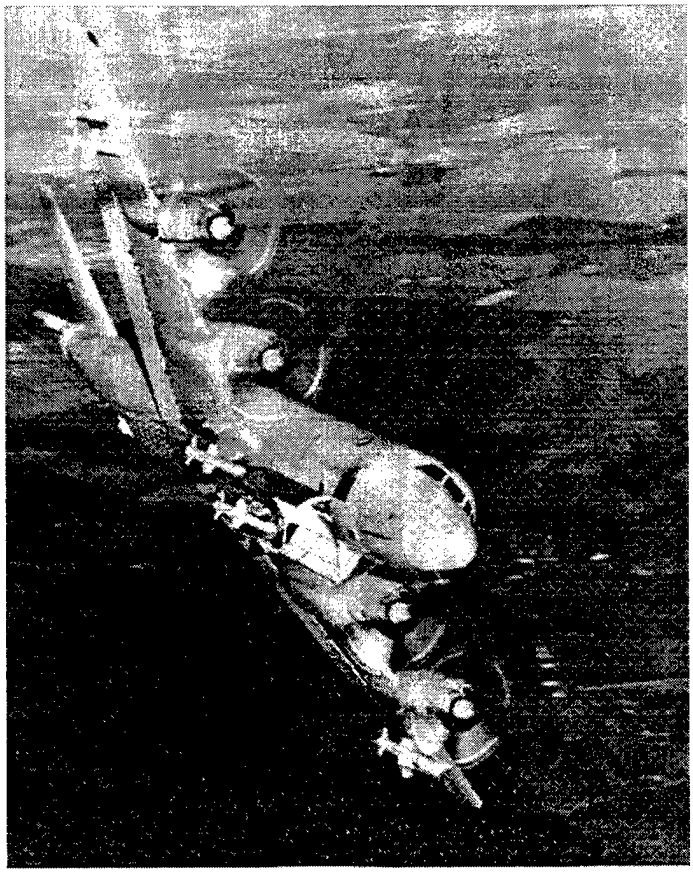

Figure I-1. P3-C "Orion" Aircraft.

operation. This investigation specifically addresses the reliability of the main landing gear lower drag struts, which have experienced the most severe surface corrosion and are currently being replaced during aircraft rework at higher than expected rates. Finite element analysis (FEA), with a probabilistic approach, and identification of a direct filtering technique for weak struts were combined to provide the decision maker with a quantitative risk assessment tool.

B. LANDING GEAR DRAG STRUT

Each P-3C landing gear consists of dual wheels with forward retracting struts, as shown in Figure I-2. The main struts on each of the three gear support the weight of the aircraft. The drag struts hold the main struts in place by carrying transverse loads from conditions such as wheel spin-up during landing and braking in both forward and reverse directions. The drag struts are hollow, tapered cylinders made from AISI 4340 steel forgings, flash welded together in the middle, as shown in Figure I-3. There are small holes left in the ends of the enclosed portion of the strut so that hot gases can escape during the flash welding process. The tapered ends are machined into lugs that hold balls for attachment to neighboring hardware thus putting the drag strut in a pin-ended boundary condition.

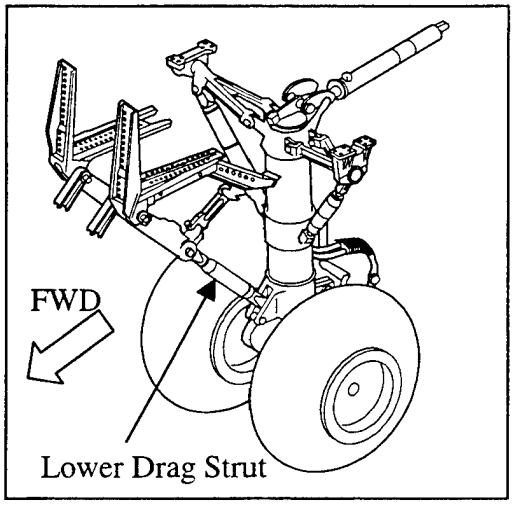

Figure I-2. P-3C Main Landing Gear Arrangement

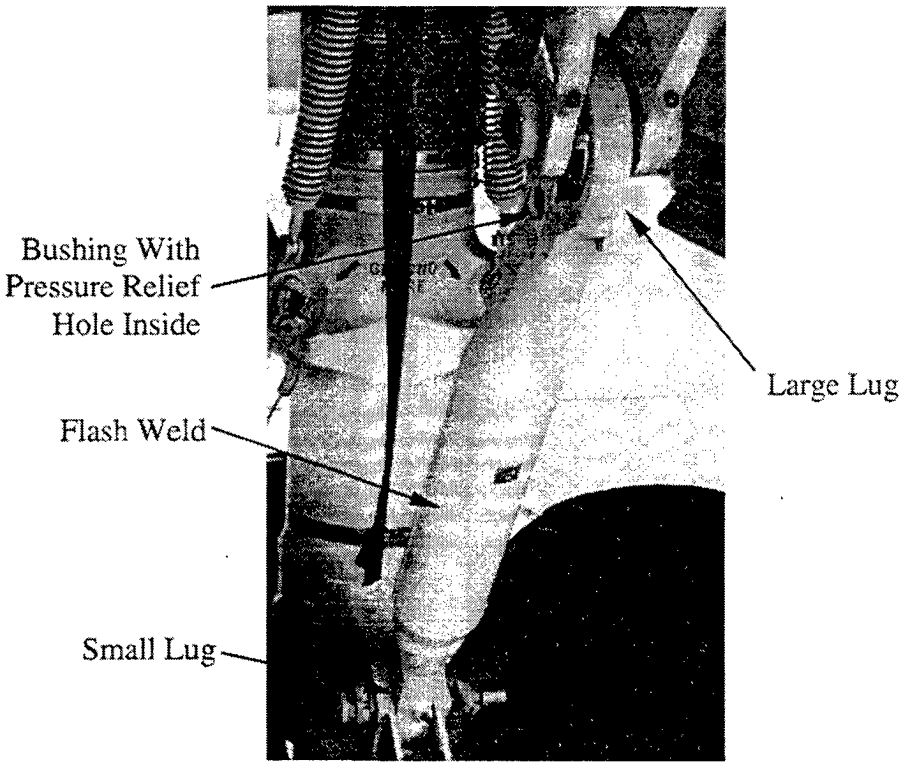

Figure I-3. Main Landing Gear Lower Drag Strut.

The P-3C is currently being overhauled under the Sustained Readiness Program (SRP) to improve the reliability of the aircraft to allow it to safely fly up to the specified original service life period. The main landing gear lower drag strut is one of many components that are inspected during SRP. One of the drag struts that was rejected during this inspection process was sent to the Naval Postgraduate School (NPS) for use in this investigation. This strut, referred to as the sample strut in the remainder of this report, was evaluated at NPS by the author to extract required data using the detailed procedures described in Appendix A.

C. LOADING

The various takeoff, landing, and taxi operations that the P-3C experiences in operation place the drag strut in both tension and compression. The maximum tension condition occurs during two wheeled braking at high speed with a defined limit load of 160,571 lbs. The maximum compression condition occurs during two wheeled braking

while the aircraft is backing down following the use of reverse thrust, with a defined limit load of 132,589 lbs. The likelihood of occurrence of this condition is extremely remote because the Navy trains its pilots not to use wheel brakes to stop the aircraft while backing down. The next highest compression load occurs during landing when the landing gear spring back following initial contact with the runway. This limit load is defined as 80,033 lbs. These loading conditions are for a heavyweight aircraft and were obtained from Lockheed Report (LR) 13680. [Ref. 1]

D. FAILURE MODES

There are three basic ways, or modes, in which the drag strut could potentially fail in service. (1) Under the tension loading condition, the strut could fracture due to fatigue cracking or manufacturing defect. This would be a catastrophic failure that would cause collapse of the main landing gear. (2) Under the compression loading condition the strut could experience column buckling, followed by gross plastic deformation. This sort of damage would more than likely cause only partial collapse of the landing gear because there would still be a physical connection between the components. (3) The strut could simply plastically yield in a way that the landing gear geometry would be altered such that the retraction, extension, or locking processes would not function properly. This investigation specifically addresses the column buckling failure mode by analysis and suggests direct filtering by low temperature proof test to address the fracture and plastic yielding modes.

E. INTERNAL CORROSION

Because of the pressure relief holes in the ends of the strut, the interior is open to the environment and subjected to atmospheric conditions as the aircraft climbs and descends. Moist air condenses on the interior surfaces of the strut and eventually causes surface corrosion. The original Lockheed design included a synthetic rubber coating on the interior surface to prevent this sort of corrosion. Over the years, several depot or factory level preventative maintenance procedures have been incorporated to solve other structural reliability issues, including hydrogen embrittlement and surface stress relief

following machining. These procedures call for baking the strut at temperatures of up to 400 degrees Fahrenheit which destroys the synthetic rubber coating on the interior [Ref. 2]. Once the coating is destroyed, the accumulation of moisture provides an environment conducive to corrosion.

F. CORROSION CHARACTERIZATION

The corrosion found in the sample rejected drag strut had several notable characteristics. An example of a semi-cylindrical section of the strut with flaking surface corrosion is shown in Figure I-4. Once the scale was removed, the pitting found on the surface was generally grouped in three spatial locations on the thin walled, cylindrical, middle section of the strut. The three locations, indicated in Figure I-5, corresponded to regions where moisture could naturally accumulate during different phases of operation on the aircraft. These regions would either be on the top or bottom of the cylindrical section depending on whether the landing gear were extended or retracted. The observed pattern was consistent with the general understanding of the corrosion process as described in Appendix B. Specifically, the observed locations were regions where water would pool on the lower surface or water vapor would condense on the upper surface. In the corrosion process, the presence and longevity of moisture on a surface is directly related to the level of subsequent corrosion. There was virtually no corrosion on the regions that would be on the sides of the cylindrical section.

The small pits were generally semi-spherical in shape to the naked eye with highly irregular boundaries when viewed through a microscope. The larger pits appeared to have been formed when the smaller spherical pits grew together. Their irregular boundaries were visible without the aid of a microscope and appeared to be influenced by the molecular imperfections in the material itself. Some of the pits were broad and shallow while others where very narrow and deep. Quantifiable characteristics of the corrosion including, pit depth, pit volume, and pit location were measured and are included in Appendix A.

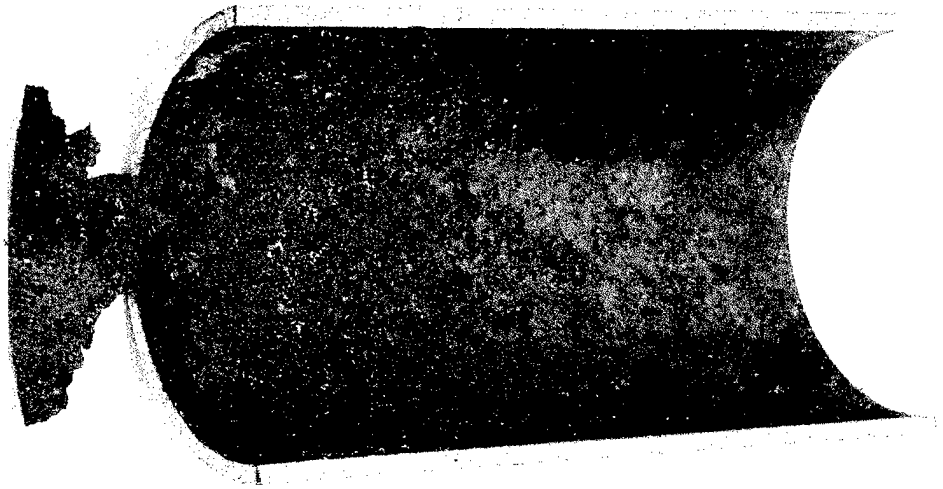

Figure I-4. Semi-Cylindrical Section With Flaking Corrosion.

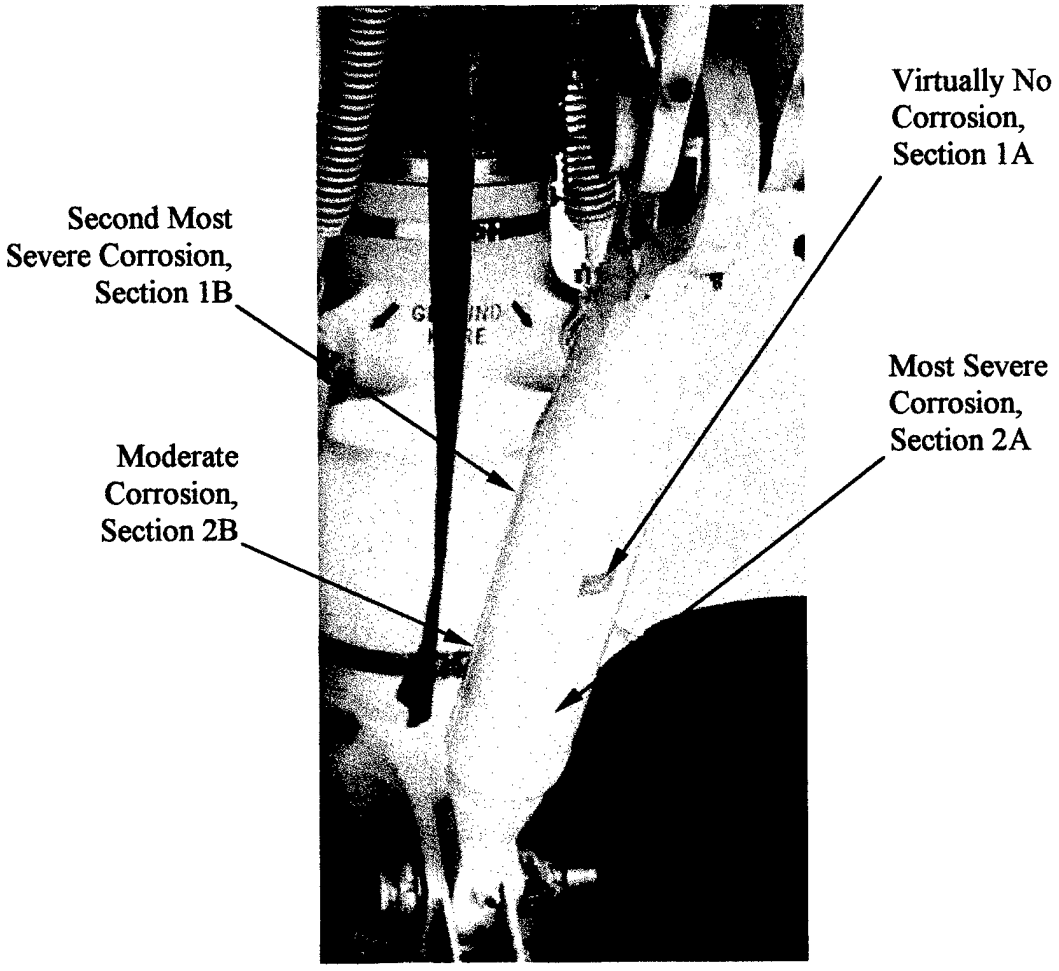

Figure I-5. Regions of Corrosive Pitting Concentration.

G. CURRENT INSPECTION TECHNIQUES

At the time of this investigation, the Navy was not performing an active inspection of fleet aircraft to determine the condition of drag struts in service. An inspection technique had been developed that included X-ray to identify areas of corrosion followed by ultrasonic inspection to determine wall thickness. Even by the best operators with the best equipment these methods are indirect, in that they do not measure the strength of the strut. They characterize the effect of corrosion on the strut, to a limited extent. A criterion had been established, based upon a recommendation from the manufacturer, that any strut with pitting that resulted in a wall thickness less than 0.140 inches should be rejected [Ref. 3]. Examination of the X-rays that were taken of the sample strut, and information received from the Navy's representative at the SRP contractor's plant, showed that these inspection techniques were highly unreliable for this situation. The author was told that the X-ray and ultrasonic inspections on the sample strut did not reveal pitting in excess of the current rejection criteria; however, the strut was rejected on a "gut feel" because a "very unusual pit" was detected. Dissection and examination of the sample strut revealed that at least 34 pits existed that were in excess of the current rejection criteria. The minimum wall thickness was found to be 0.122 inches.

H. ANALYSIS METHODOLOGY

The methodology used in this analysis has been summarized in Figure I-6 which is a flow chart of the steps necessary to arrive at the ultimate risk assessment.

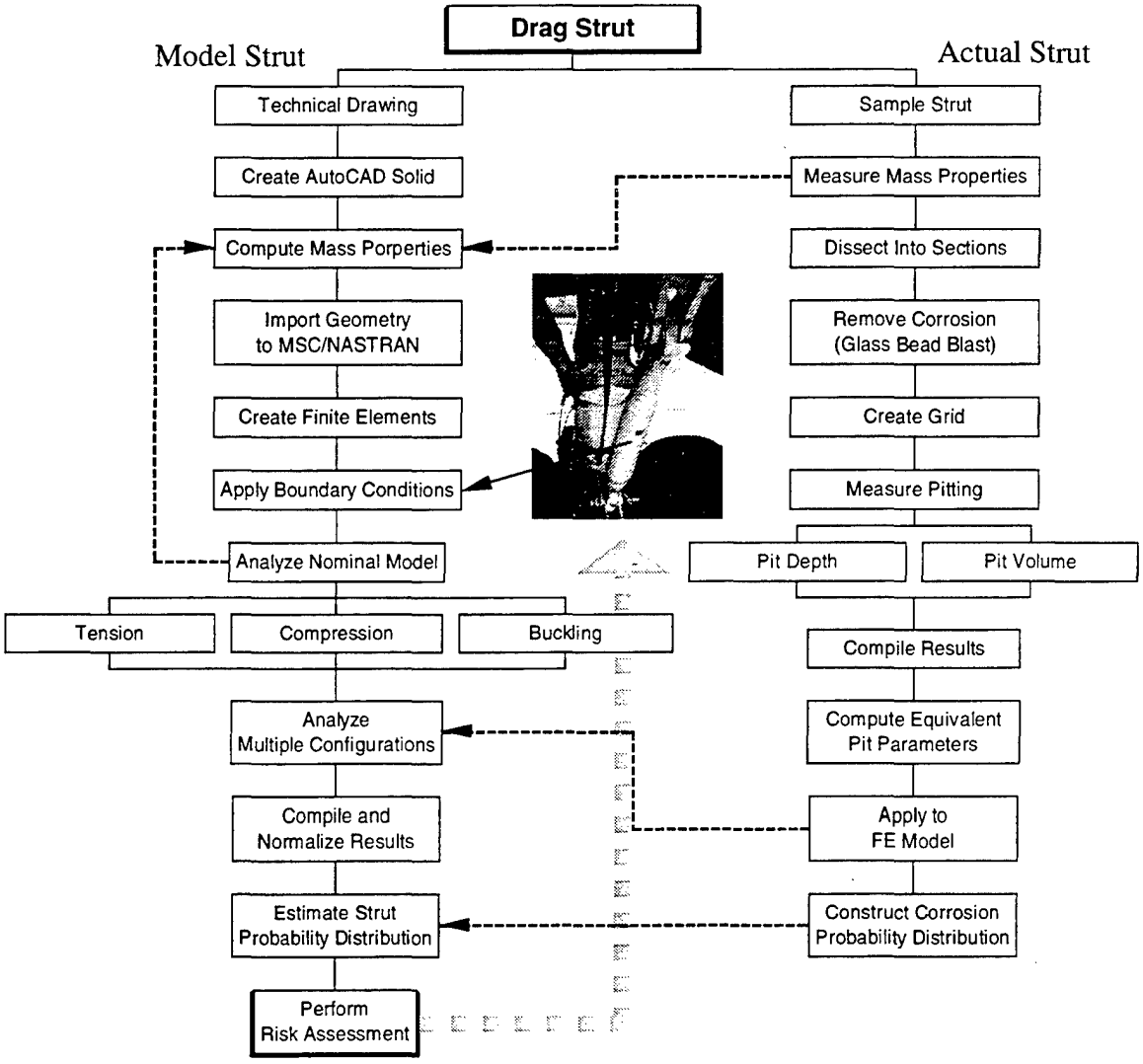

Figure I-6. Risk Assessment Methodology Flow Chart.

II. PROBABILISTIC RELIABILITY

A. CONTINUOUS RANDOM VARIABLES

To determine the reliability of a component such as the drag strut one must recognize that there is a finite population of drag struts in existence. The population has distinct characteristics, or properties, in terms of many different variables such as strength, weight, physical dimensions, levels of corrosion, etcetera. These variables are random, or stochastic, because there is no predetermined order or exact set of values for the variables in any given strut. The variables are continuous because they can take on any value within certain bounds described by the geometry, materials, and manufacturing processes that make up the strut. Each individual drag strut has its own levels of these continuous random variables (RV). There are mean, or average, values for an individual strut but different values at any given location within the strut. There is no way to predict the exact levels of these variables; however, one can put bounds on the levels given some knowledge about the population. More importantly, one can establish the probability of finding a particular strut with a given level of one of these variables if the probability distribution function for the population is known.

B. PROBABILITY DISTRIBUTIONS

Let the probability of finding a discrete value x, of some random variable X, be given by $P(X = x) = f(x)$, where $f(x)$ is called the probability distribution function. In probability distributions of continuous RVs, the probability that a given variable X takes on any one discrete value is generally zero. However, one can determine the probability that X lies between two different values and thus the probability distribution for a continuous RV can be found. A real-valued RV must definitely lie between $-\infty$ and ∞, and the sum of all the probabilities must equal unity, because the entire population is being considered. These statements are represented by:

$$f(x) \geq 0 \tag{1}$$

$$\int_{-\infty}^{\infty} f(x)\,dx = 1 \tag{2}$$

$$P(a < X < b) = \int_{a}^{b} f(x)\,dx \tag{3}$$

The probability that the random variable X takes on at least some value x is given by the cumulative distribution function (CDF) $F(x)$, where

$$F(x) = P(X \le x) = P(-\infty < X \le x) = \int_{-\infty}^{x} f(u)\,du \tag{4}$$

C. DISCRETE RANDOM VARIABLES

Continuous RVs are fine for mathematical relationships; however one can only measure or quantify discrete values of random variables when dealing with a real object. The discrete values are dependent upon the scale, or resolution, of the instrument used to measure or evaluate the object. If the scale is small enough, then the attributes of the discrete RV approach that of the continuous. In this case, the summation of all of the measured discrete values of the RV must be unity, because the entire population is being considered. This is represented by:

$$\sum_{x} f(x) = 1 \tag{5}$$

The remainder of this investigation deals with discrete RVs. In each case, the scale was chosen as a compromise between physical limitations of measuring tools, the time available to quantify the RV, and a desire to represent the real continuous RV as closely as possible.

D. SPECIFIC DISCRETIZED RANDOM VARIABLES

The drag strut, as originally manufactured, was thought to be reliable enough for the planned service life of the aircraft. To date, there have reportedly been no in-service structural failures, which validates the original analysis. However, that analysis did not consider the effect of corrosion because that damage process had been precluded by the synthetic rubber coating. The RVs that were important for determining the original strut reliability were controlled during the manufacturing process. The material had to meet

certain specifications in terms of hardness, modulus of elasticity, ultimate strength, etcetera. The strut had to be machined to within certain dimensional tolerances and the flash weld had to be performed under specific process specifications. Finally the manufactured strut was proof tested in tension at room temperature, which served as a high pass filtering process to remove any weak struts that slipped by the other control mechanisms. The proof test load was set at 67 percent of the material yield strength or 220,600 pounds and was specifically intended to assure the reliability of the flash weld [Ref. 4]. The RVs that are important for determining corroded strut reliability have now been augmented by things relevant to the corrosion damage process. They differ from the original RVs in that their levels can not be controlled, but only evaluated. The augmented RVs, or corrosion induced effects, can be characterized by either the spatial location of one or more damage sites on the strut, or the individual attributes of any one damage site. These damage sites will be referred to as pits from this point forward.

1. Pit Spatial Location

a. Single Pit

There are infinitely many spatial locations for pits within the strut because location is a continuous RV. Location had to be converted to a discrete RV for characterization and analysis. The critical part of the strut for resistance to column buckling is the thin walled cylindrical portion in the middle. This portion was divided into four semi-cylindrical sections as shown in Appendix A. These sections were further subdivided into an 18 by 24 grid that contained 432 possible locations. These locations will be referred to as grid elements or just grids in the remainder of this document. But column buckling is particularly sensitive to imperfections at critical locations; specifically the anti-nodes of the harmonic modes. For this reason, special emphasis was given to cases where the worst pits were located at critical nodes. This reduced the number of combinations to be analyzed to a manageable level.

b. Pit Clustering or Multiple Pits

When considering multiple pits within the discrete location RV, there are still more possible combinations of pits than could be evaluated in this investigation. Because the order in which the locations were selected was not important, the number of combinations possible could be calculated from the following formula for combinations of n things taken r at a time:

$$ {}_nC_r = \binom{n}{r} = \frac{n!}{r!(n-r)!} \quad : \quad n! = n(n-1)(n-2)\cdots 1 \tag{6} $$

If two pits were considered, there would be 93,096 combinations of pit spatial location. For three pits, there would be over 13 million combinations. These numbers are for only one kind of pit. If pits of different characteristics were coupled together with the possible location combinations, the numbers would get even larger. To deal with this, a series of extreme cases were chosen. The analysis progressed from pits to through-the-thickness holes of increasing diameter, up to a maximum of two inches. The holes were assumed to be a practical determination of the worst possible case, i.e., no operator would miss or accept a two inch hole in the side of any strut.

2. Pit Attributes

There are multiple attributes that could be used to describe the corrosive pits found within the drag strut. Each of them is a continuous RV in its own right which has to be discretized in order to be used in analysis. The following attributes were chosen on the basis that they would have a distinct impact on the strength or reliability of the strut. The detailed procedures used to extract the values of these parameters in the sample drag strut can be found in Appendix A.

a. Pit Depth

This was the easiest attribute to quantify because it could be measured directly. There was no special technique required to evaluate the impact of pit depth. In other words, a deep pit is worse than a shallow pit because there is a direct reduction in

the amount of material present to carry stress within that grid. Each grid element was discretized by the depth of the deepest pit within that grid.

b. Pit Volume

The volume of material missing due to corrosion was more difficult to quantify because it could not be measured directly. Instead, the amount of liquid required to fill the pits in each grid was measured. Alcohol was chosen for this because of its low surface tension which allowed it to spread evenly across the pits and not bead up. This attribute should also directly relate to the strength of the strut because of the reduction in material present to carry stress and provide stability.

c. Pit Shape

The shape of individual pits would have a significant impact on a fracture mechanics or fatigue life analysis. However, column buckling is more sensitive to the overall cross-section moment of inertia and the overall distribution of material, not the shape of a single pit on the interior surface. Because the fracture and fatigue failure modes are being addressed by proof test, except for observing the general nature of pit shape and growth as described above, there was no attempt to record the pit shape in each grid.

d. Equivalent Spherical Pit Radius

One goal of the pit attribute definition process was to provide a means for modeling corrosion with finite elements (FE). To this end, a single parameter was required to combine both the pit depth and pit volume. The chosen parameter was equivalent spherical pit radius. This was the radius of a sphere such that a slice from that sphere, at a depth equal to the grid pit depth, would occupy the same volume as the grid pit volume. This is more clearly illustrated in Figure II-1, where R is the equivalent spherical pit radius, h is the pit depth and V is the pit volume. The justification for the choice of this attribute in terms of corrosion pit propagation is included in Appendix B.

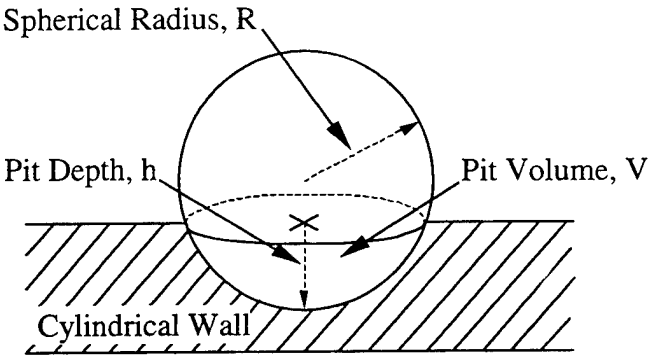

Figure II-1. Equivalent Spherical Pit Radius.

e. Pit Severity

The final attribute used to quantify corrosion in the strut was defined as pit severity, which is simply the grid pit depth multiplied by the grid pit volume. It is somewhat like using the first moment of mass to find the centroid of a solid. The contribution of an individual element to the centroid of the object depends upon its mass and its distance from the origin. In this case, the contribution of pitting in an individual grid to the strength of the strut depends upon the volume of material missing and its distance from the surface. This attribute was needed so that a probability distribution could be developed that would accurately describe the chances of finding a certain level of corrosion in a certain location. The assumption was that the statistics of finding corrosion at any grid location (for the sample strut) could be generalized to be the probability of occurrence of corrosion severity at any location, within any strut, from any P-3 aircraft. This thought is based upon fractal theory; or the idea that within a population of drag struts, the map of the corrosion severity within a strut can be duplicated in any other strut from the population. All that is required is the appropriate scale for the map, or in this case the grid. The justification is that the sample strut came from the population subset of rejected struts. It contains the character of the worst (because it was rejected) and there is a distinct distribution of corrosion (not uniform corrosion all over).

E. PIT SEVERITY PROBABILITY DISTRIBUTION

The pit severity at each grid location was plotted as a 3D surface as shown in Figure II-2. The plot has been oriented to allow viewing orthogonal to the xy plane (location axes), with 10 levels of color providing discrimination along the z axis (pit severity). Each of the 432 grid boxes was further divided into fifths to provide additional resolution in location. The number of fifth grids at each of the 10 levels of pit severity was counted and then normalized by the total number of fifth grids or 2,160. The result is the frequency of occurrence of all the different levels of severity within the cylindrical portion of the strut. Because this frequency of occurrence has been normalized by the total number of fifth grid elements, it also meets the requirements of a probability

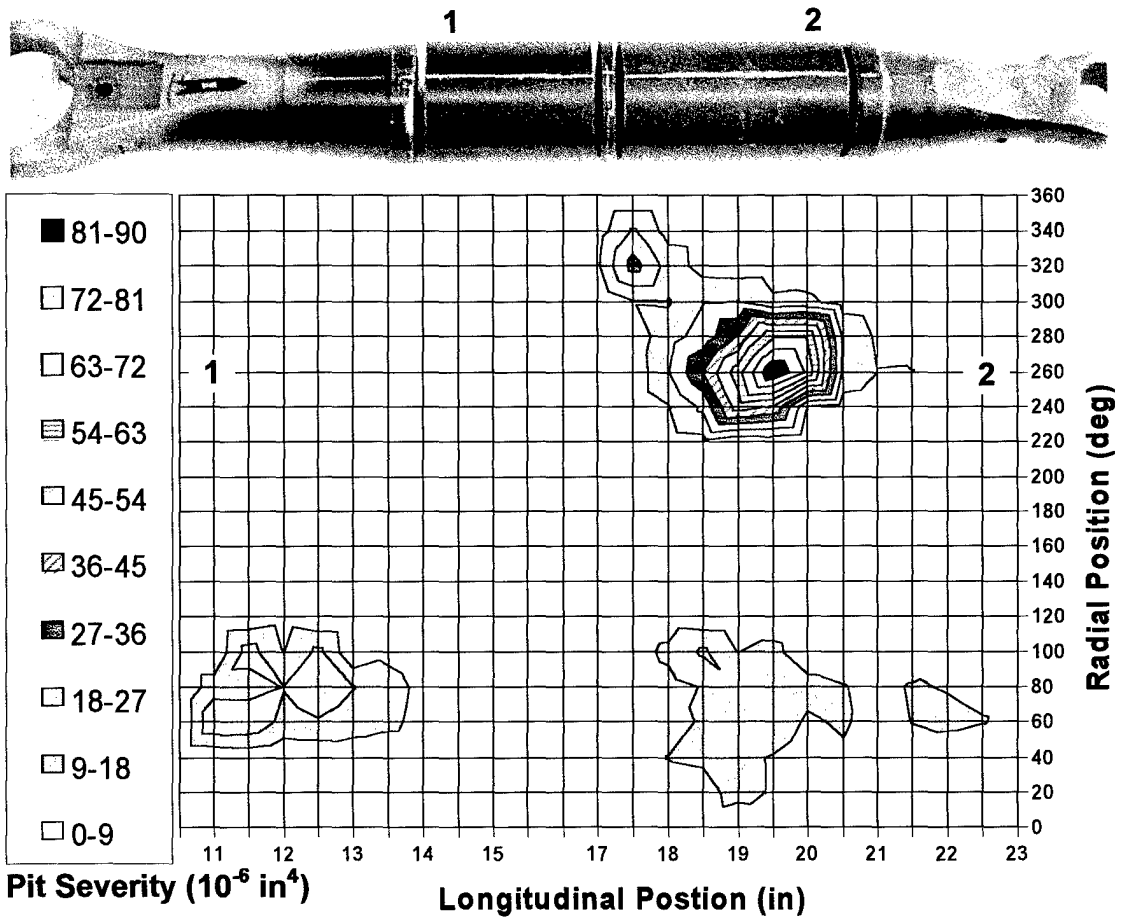

Figure II-2. Pit Severity Distribution Surface Plot.

distribution. The result is a probability distribution of corrosion severity in the cylindrical section of the strut. Recognizing that a multiplicative relationship exists in the definition of pit severity and the corrosion process in general the frequency of occurrence data was plotted in natural log space. This allowed determination of the mean and standard deviation for a normal distribution, which could then be transformed back to regular severity space. The result would be a lognormal distribution of the probability of finding a pit of a certain severity in any given drag strut. Figures II-3 and II-4 show the results of this process, including the equations for the respective distributions. The ten individual levels of severity are plotted as circles, representing a histogram of all the grid severity measurements. The reason there are no points on the left of the normal distribution in the natural log space is that pits with severity at that level would be at the microscopic level, as indicated by the relative size icons at the bottom of Figure II-3.

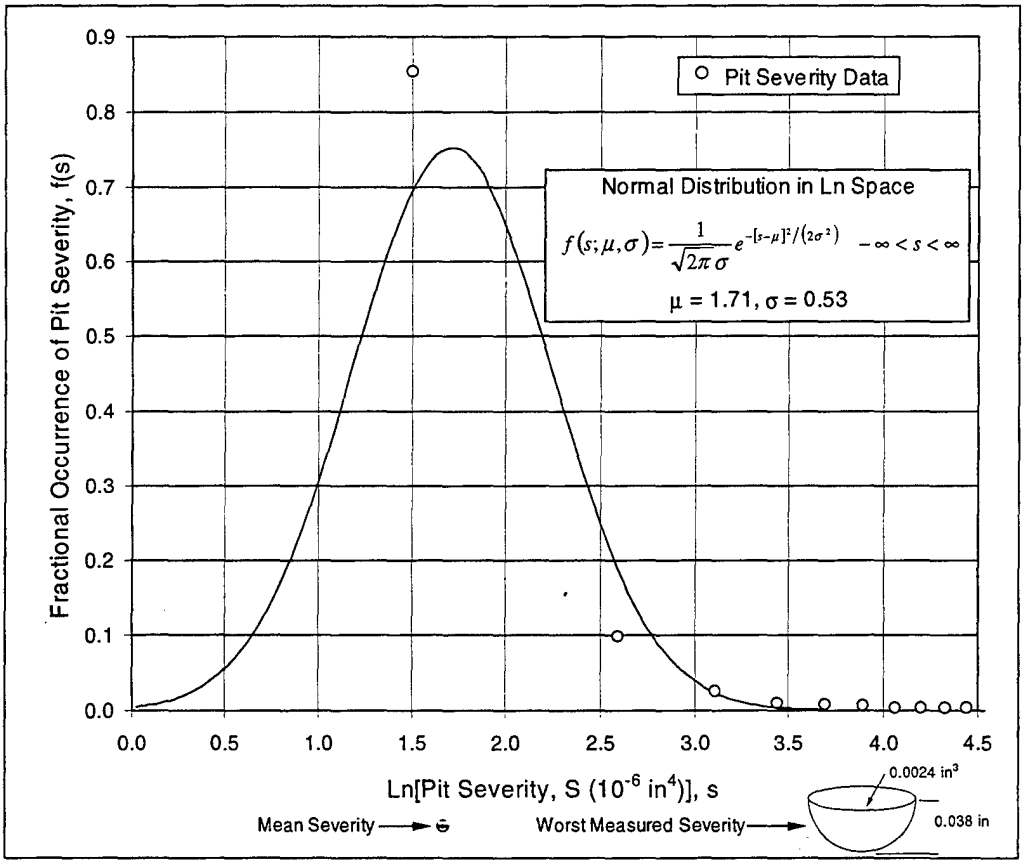

Figure II-3. Fractional Occurrence of Severity in Natural Log Space.

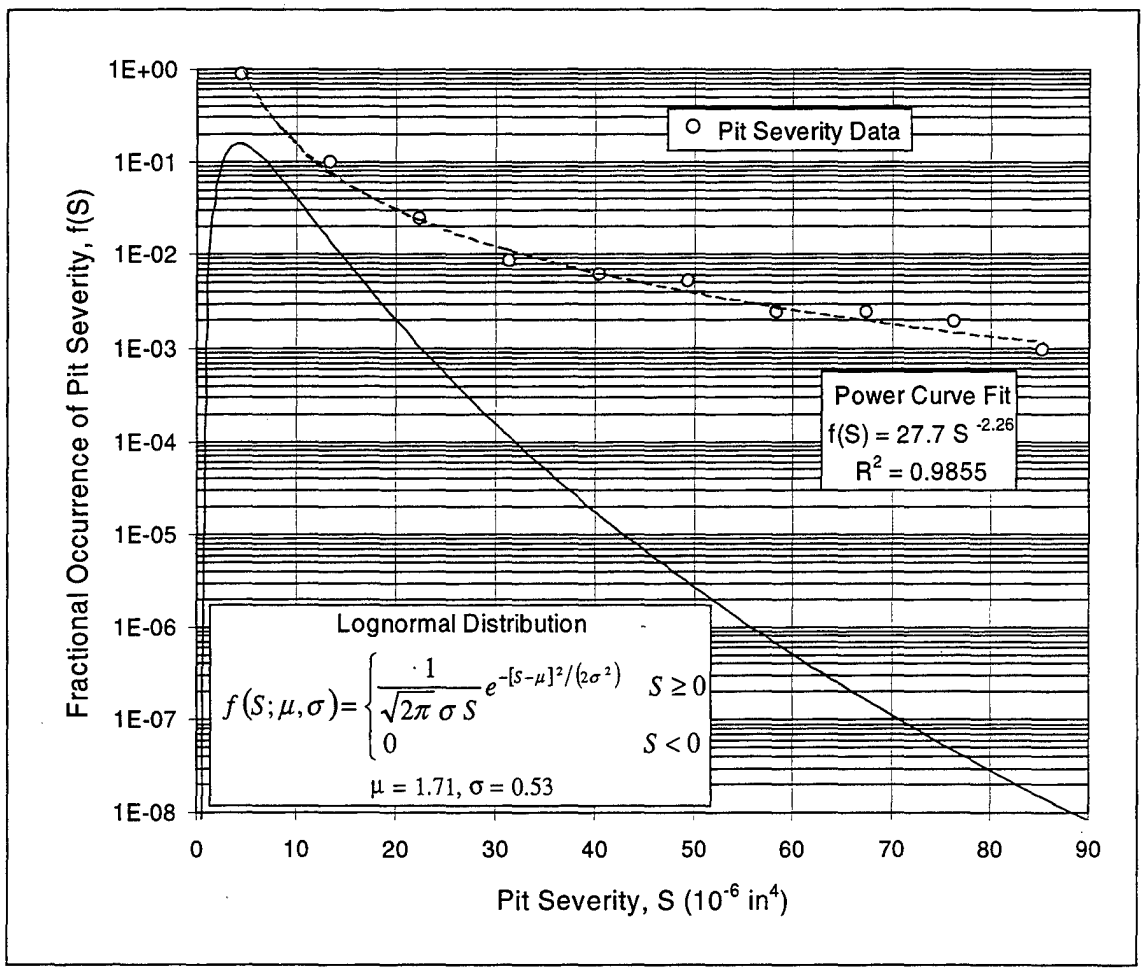

Figure II-4. Fractional Occurrence of Severity.

The significance of this distribution is in the probability of finding the worst pit in any strut. Over time, the right tail of the distribution will shift to the right, i.e. the rare or worst pits will get worse. The area on the left (small or common pits) will be redistributed as the overall level of corrosion increases, but the probability of occurrence of the rare pit will basically stay the same. Based on the fractional measurement of the current sample strut, the probability of finding the worst pit, or *P(S),* was determined to be 0.00093. In addition to the lognormal distribution, a power fit relationship was determined as an estimate of the upper tail probabilities, because the lognormal clearly does not sufficiently model what was observed. Because a power fit has been used, a more clear representation of the function, and the required extrapolation to far greater

levels of severity can be seen using a log-log scale, as is shown in Figure II-5. The power fit has been extrapolated and could now be used to determine the probability of finding the extreme case (worse corrosion, but less frequency of occurrence).

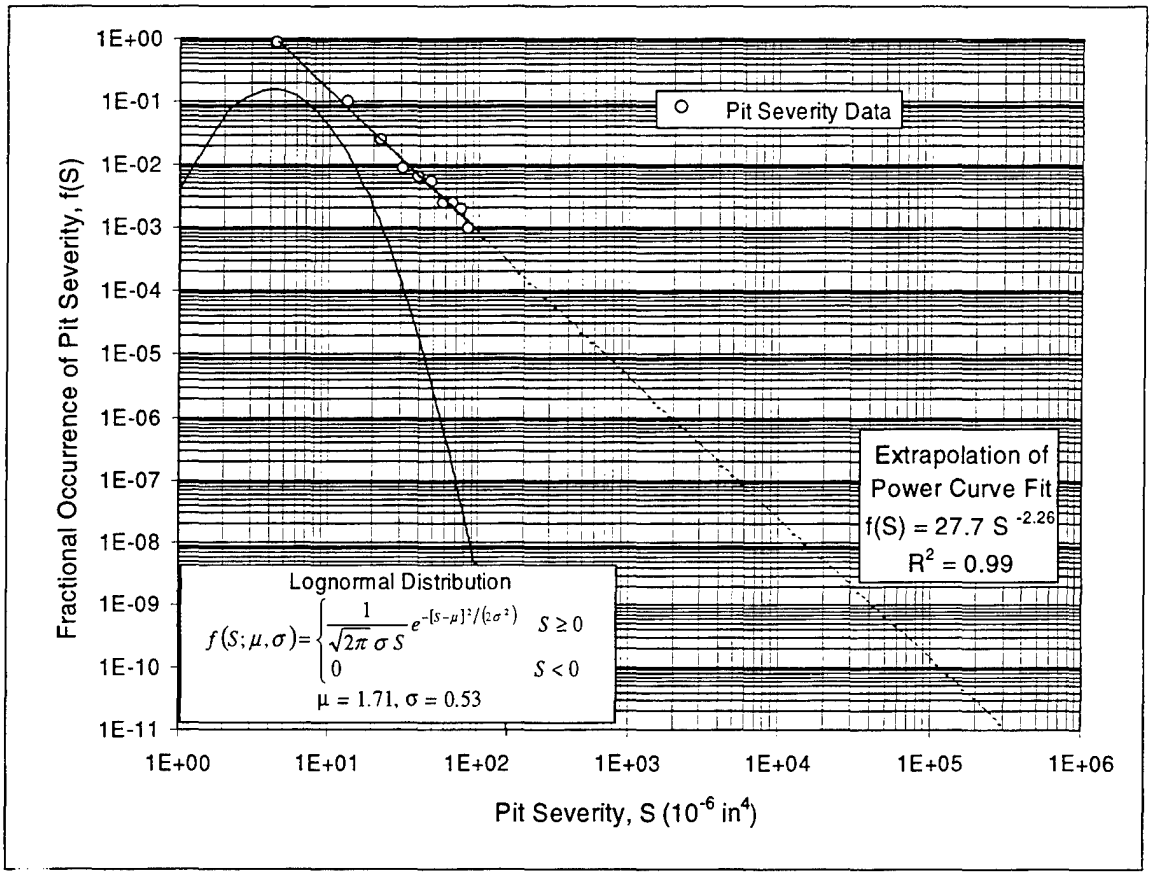

Figure II-5. Extrapolation of Fractional Occurrence of Severity.

The next step was to determine the probability of finding a pit at any given location within the strut. The pitting was assumed to be independent and identically distributed (iid), i.e., the probability of occurrence of a pit at a certain location in the strut did not depend on any of the other pits in the strut and pitting was equally likely to occur at any location. This actually added some conservatism to the analysis because the pitting distribution in the sample strut was not observed to be equally likely; specifically there was no pitting observed in critical locations. However this assumption was necessary to enable the continuation of the probability model. Because there were 432

equally likely grid elements, then the probability of finding a pit in any grid, or *P(L),* was $\frac{1}{432}$ or 0.0023.

Finally, the probability of finding both the worst pit and of finding it at a specific location was the joint probability or $P(S \cap L)$. A joint probability can be represented by:

$$P(A \cap B) = P(A)\,P(B \mid A) \tag{7}$$

where *P(B|A)* is the conditional probability, or the probability of *B* occurring given that *A* has already occurred. When the "iid" assumption is made, the conditional probability simply becomes the *P(B)* and the joint probability becomes the product of the two. Thus $P(S \cap L)$ becomes the product of *P(S)* and *P(L)* or 2.15 x 10^{-6}.

The crucial question in determining the column buckling reliability of the drag strut in the presence of corrosion was: What is the probability of finding a pit bad enough, and in a critical location, to cause buckling in any given strut? The answer to this question was formulated through realization of a single random variable by finite elements. Models of far more severe corrosion than observed in the sample strut were created, and the probability of occurrence of those configurations were determined from the joint probability using the product of the power fit of probability of severity and the probability of location as discussed above. This physically enormously complex multivariate problem has been reduced to a single characteristic random variable encapsulating the effect on buckling by the joint attributes of all the variables.

F. RANDOM VARIABLE REALIZATION BY FINITE ELEMENTS

The key to doing a risk assessment of the strut in buckling was to be able to relate the analysis to a random variable that had meaning to the operator or decision maker. The envelope within which the aircraft is operated is defined by various limitations. These limitations may be in terms of airspeeds, accelerations, landing sink rates, etcetera. The manufacturer had done the work of translating these limitations into service loads (forces or moments) on individual components, in this case the drag strut. Therefore, all that was required was a realized random variable with a probability distribution that was in terms of load, which in turn can be related back to operational conditions.

There were at least two ways to accumulate the statistics of a realized random variable in terms of load: (1) by actual buckling testing of real struts or (2) by finite element analysis. In this investigation, FEA was used to perform a virtual realization of a random variable in terms of critical buckling load. This was done by mapping all of the attributes described above into a single random variable (which is a measurable quantity) and then finding the strength (the realized random variable) by finite elements. This made it possible to relate the service load to the critical buckling load in probability terms and hence, perform a risk assessment as will be presented later in this report.

III. APPLICATION OF FINITE ELEMENTS

A. ASSURANCE OF COMPUTATIONAL RESULTS

In the beginning of this investigation, certain assumptions were made concerning the maturity of finite element analysis. The goal was to provide the decision maker some analysis results that could be taken at face value, with an obvious visualization of the problem and its solution. Therefore, the investigation was guided away from the classical technique reducing the problem to something that could be manually calculated through idealizations and assumptions. In that case, the problem is pragmatically idealized to match available solution techniques. As a result, the solution is accurate but the interpretation of the results requires a great deal of study and understanding to extend the results back to the real world. Instead, in this investigation the opposite route was taken, that is: a complex model, that closely matched the real strut was constructed and a sophisticated analysis was relied upon to provide results that could be directly applied to the real world.

MSC/NASTRAN[1] was selected because it was a well tested and established software application, and it could perform the automatic solid meshing required to represent the drag strut with finite elements. NASTRAN was used as an application package; that is, no effort was expended in element development. A more simple geometric model of the cylindrical portion of the strut could have been used, but the analysis would have required additional compromise in forming the equivalent boundary conditions. The interpretation of results would be ambiguous because the simpler model would need to be related back to the actual strut. This approach was not used. Instead, extensive effort was expended to assure the geometric model was a duplication of reality; thereby enabling the use of actual boundary conditions and results that could be used without interpretation. The high degree of replication of the physical drag strut by geometric model can be seen in the modeling section to follow, say Figure IV-1. With

[1] MSC/ is a registered trademark and service mark of The MacNeal-Schwendler Corporation. NASTRAN is a registered trademark of the National Aeronautics and Space Administration.

that in mind, the following paragraphs explore some of the details of FEA that are germane to the results obtained and provide a level of assurance that the results are valid.

B. LINEAR ELASTIC BUCKLING

The analysis of the drag strut in this investigation was performed assuming linear elastic behavior of the material under load. In linear static analysis, a state of stable equilibrium is assumed at all times. The structure deforms under load in a linear fashion, and the displacements are determined directly from the properties of the material being modeled; specifically the elastic modulus. When the load is removed, the structure is assumed to return to the undeformed position. In the case of linear buckling analysis, the solution process continues until the assumption of stable equilibrium is no longer satisfied. In other words, at some point the loading condition will be such that the deformation increases without any increase in load. The structure has become unstable and has reached the bifurcation point. It is assumed that there is no yielding of the structure up to this point and the direction of the applied load has not changed.

The key to finite element analysis is the stiffness matrix. The stiffness matrix is determined from the geometry of the model and the properties of the elements that make up the model. Included in the properties of the elements are the characteristics of the material that the element is representing, in this case the modulus of elasticity and Poisson ratio. The size of the stiffness matrix is determined by the complexity of the model (the number of nodes) and the degrees of freedom allowed for each node. The stiffness matrix is the minimum potential energy of all the nodal displacements in static equilibrium. Elastic buckling analysis in NASTRAN includes the effect of differential stiffness. This allows for higher order strain displacement relationships that are functions of geometry, element type, and applied loads. This can be viewed as a linear approximation of softening the stiffness matrix under compressive load. It is this softening effect that leads to the point of instability in the structure.

C. EIGENVALUE DECOMPOSITION

The finite element solution for linear buckling is determined by finding the eigenvalues of the stiffness matrix. The eigenvalues are scale factors that multiply the applied load in order to produce the critical buckling load. The eigenvalue is the characteristic value of the stiffness matrix such that the effect of the differential stiffness matrix has caused the stability of the structure to reach zero. This is the point of instability. Mathematically, the eigenvalue is the value that causes the determinant of the stiffness matrix to go to zero. The process of finding this eigenvalue is called decomposition in matrix algebra terms. There are many eigenvalues that will result in this point of instability; as many as the number of rows or columns in the stiffness matrix since it is a square matrix. Generally, only the smallest eigenvalue is of interest because this is the lowest load at which the structure will become unstable. The buckling eigenvalue problem reduces to:

$$[K + \lambda_i K_d] = 0 \tag{8}$$

where K is the stiffness matrix, K_d is the differential stiffness matrix, and the λ_i are the eigenvalues to be computed. Once the eigenvalues are determined, the critical buckling load is found from:

$$P_{cr_i} = \lambda_i P_a \tag{9}$$

where P_{cr_i} are the critical buckling loads and P_a is the applied load.

NASTRAN incorporates three methods of eigenvalue decomposition for buckling analysis because no single method is perfect for all matrices. As the size of the matrix increases, or if the matrix is ill-conditioned, the manipulation of all of the terms in the matrix to find a solution leads to computer round-off errors and division by zero. The methods used are Lanczos, Inverse Power, and Sturm Modified Inverse Power [Ref. 5].

D. CONVERGENCE OF ANALYSIS RESULTS

As described by Bathe [Ref. 6], FEA requires the idealization of actual physical problems into mechanical descriptions, followed by finite element solutions of the idealization. He states, "...a proper FE solution should converge (as the number of

elements is increased) to the analytical (exact) solution of the differential equations that govern the response of the mechanical idealization." Bathe goes on to highlight the sources of error in a FEA which include "discretization, numerical integration in space, evaluation of constitutive relations, solution of dynamic equilibrium equations, solution of FE equations by iteration, and round-off error." [Ref. 6, p. 165, Fig. 4.23, Table 4.4] In light of this, it was assumed that if an accurate and complex mechanical idealization of a real strut was used as an input, and a FEA converged, an accurate solution of the buckling load should result. The accuracy of the mechanical idealization was validated by comparison of mass properties. It was hoped that the sources of error described above would be covered by the maturity of the FEA tool in use, namely NASTRAN.

E. MIDSIDE NODES AND CONVERGENCE

Two types of nodes used in the definition of finite elements are corner nodes and midside nodes. Corner nodes are points at which the elements connect with each other. Midside nodes can be included to provide interpolation points between the corner nodes. The convergence on a solution is greatly affected by the presence of midside nodes. Two methods of convergence used in FEA are polynomial, or P-convergence, and stepwise, or H-convergence. P-convergence, through the use of midside nodes, includes displacement interpolation between the corner nodes. The number of nodes added between the corners equals the order of the interpolation polynomial plus one. Thus, the term parabolic interpolation is used when one midside node is included on each edge of the element. This is a result of the works of B. Szabo, E. Wilson, and K. Bathe. Stepwise, or H-convergence, is by decreasing step size, i.e., element size. It is computationally efficient and appropriate for large, uncomplicated structures.

P-convergence is faster with respect to element dimensions and computational speed and less demanding on computational resources but requires more complex mathematical implementation (Rayleigh-Ritz within each element). H-convergence is slower and easier to implement, but much more computing resource demanding. The current trend is to use H-convergence because of accessibility of increased computational power. Convergence for eigenvalue decomposition is more demanding than merely

computing stresses and displacements because of the need to evaluate all possible displacements. More compliant elements converge better in eigenvalue problems because of the smooth transition from one element to the next. However, in some cases, compliant elements can lead to erroneous convergence which results is extremely convoluted displacements. An example of this can be seen in Figure III-1, which is from one of the aluminum tube buckling models discussed in Appendix D.

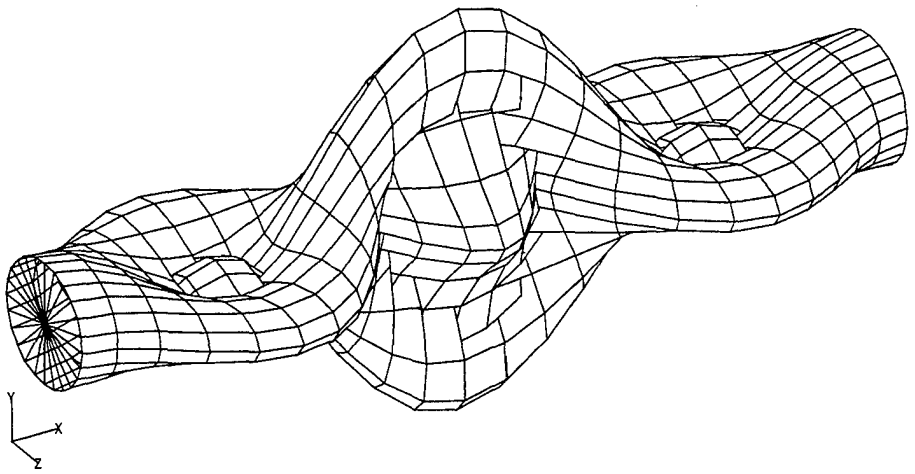

Figure III-1. Convoluted Displacement Results From NASTRAN Buckling Analysis

F. THREE DIMENSIONAL ELEMENTS

The type of element used in this analysis was a solid tetrahedron with four triangular surfaces, six edges, and four corner nodes. This type of element does not allow for rotation of the corner nodes. The result is four nodes, with three translational degrees of freedom each, for a total of 12 degrees of freedom per element. Without nodal rotations, the elements tend to interlock and are not very compliant for a given number of degrees of freedom. When midside nodes are included on the six edges, the total degrees of freedom for the individual element increases to 30. Even without nodal rotation, the effect of the midside nodes is to release the element interlocks, making the structure more compliant. The two different kinds of solid tetrahedron elements are shown in Figure III-2 below.

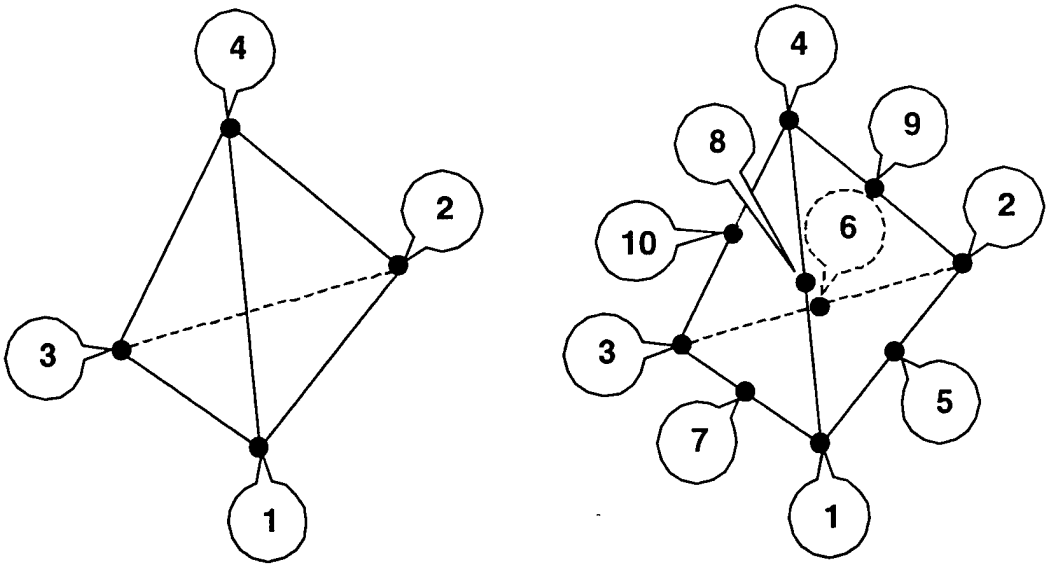

Figure III-2. Solid Tetrahedron Elements With & Without Midside Nodes.

G. ASSUMPTION OF CONSISTENT CONVERGENCE

The hypothesis was made that regardless of whether or not midside nodes were present, the eigenvalue decompositions, if they converged, would converge to consistent solutions between models with the same element characteristics. This allowed comparison of buckling loads among different configurations of drag strut corrosion models with the same element type and size. In this investigation, the corroded model buckling load is normalized by the nominal, non-corroded model buckling load. Thereby, any convergence difficulties would be self-compensating. Thus the percent reduction in buckling load from corrosion could be used even though the absolute value of the load may not be precise.

IV. MODELING

A. MODELING BY GEOMETRY

The modeling process began with the original Lockheed technical drawing used to manufacture the drag strut [Ref. 5]. The computer-aided design (CAD) software application AutoCAD[2], Release 13, was used to create a three-dimensional (3D) solid representation of the strut that matched the engineering drawing nominal dimensions. All aspects of the drawing where included in the AutoCAD model, including the various chamfer radii at surface intersections. The details of the modeling process are included in Appendix C. Figure IV-1 indicates the overall flow of the modeling process as well as the high level of replication achieved. The goal was to make the model match the real strut as closely as possible. Several protrusions on the lug ends were not included in the model because they would have only increased the complexity of the model without any contribution to the strength of hollow cylinder portion of interest in this investigation. However, the eccentricity that could exist in a manufactured strut as a result of allowable tolerances in the flash welding process was included. Close inspection of the figure shows the presence of the eccentricity at the flash weld, indicated by the arrow. The AutoCAD solid model was exported into an ACIS[3] file, which is one of many CAD industry standardized file formats for transporting 3D solid and 2D surface and curve geometries between different software applications.

B. MODELING BY FINITE ELEMENTS

The FE modeling process involved the use of the software application MSC/NASTRAN for Windows[4], Version 3.0.2. The ACIS file from AutoCAD was imported to NASTRAN as a single 3D solid geometry along with all the curves and

---

[2] AutoCAD is a registered trademark of Autodesk, Inc.

[3] ACIS is a registered trademark of Spatial Technology, Inc.

[4] Windows is a registered trademark of the Microsoft Corporation.

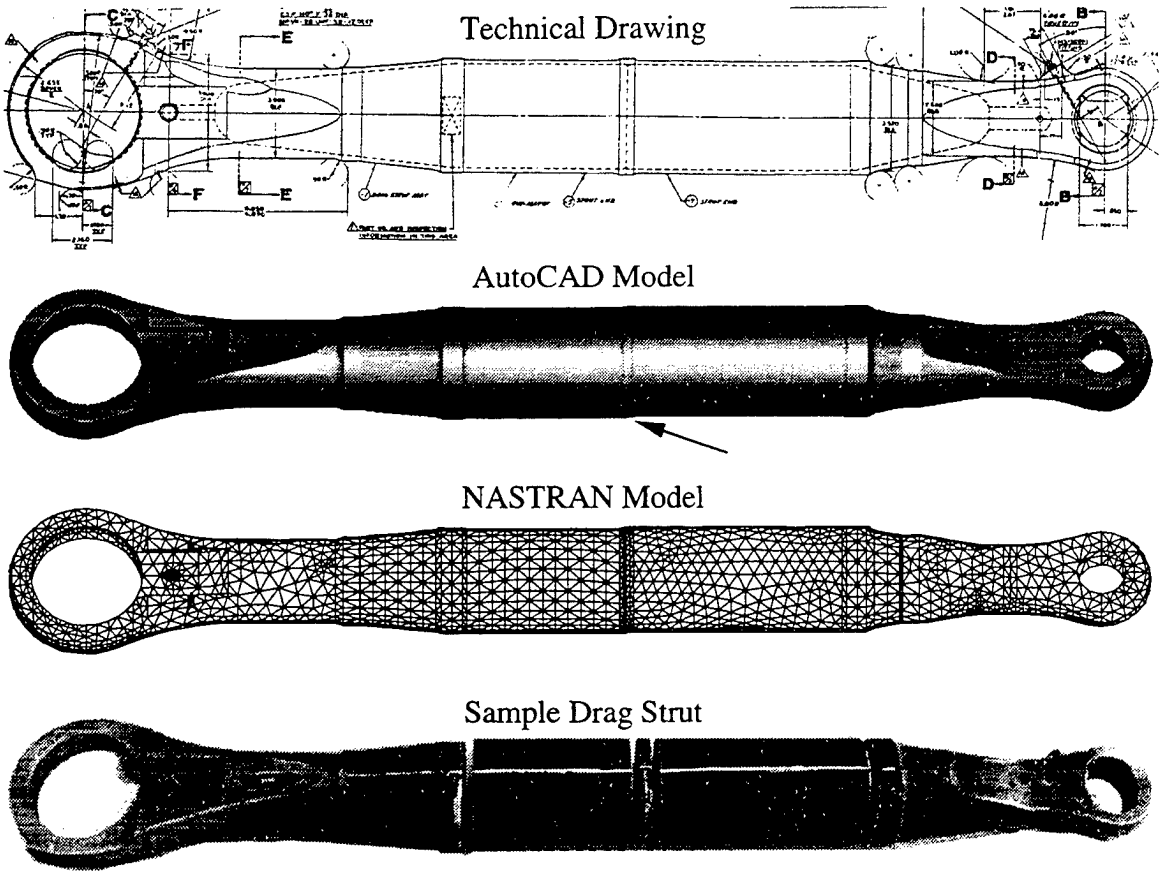

Figure IV-1. Modeling Process Flow & Sample Drag Strut.

surfaces that defined that geometry. The built-in NASTRAN solid meshing routine was used to define a grid of 3D solid tetrahedron FEs with four corner nodes each. The meshing routine could also create tetrahedron elements using six midside nodes in addition to the four corner nodes, for a total of ten nodes per element. Both types of tetrahedron elements are shown in Figure III-1. The impact of using midside nodes in the FEA process was discussed in section III above. Midside nodes were not used in this investigation because the license purchased for MSC/NASTRAN for Windows only permitted models of up to 5,000 nodes. It was not possible to model the strut with tetrahedron elements including midside nodes with only 5,000 total nodes. The maximum element size parameter was varied within the built-in meshing routine until a model of the strut was obtained with as close to 5,000 nodes as possible, leaving some room for model growth when simulated corrosion effects where included.

C. MODEL VALIDATION THROUGH MASS PROPERTIES

Both the AutoCAD and NASTRAN models were validated in terms of accurately representing the real drag strut by comparing the computed mass properties to measured values from the sample rejected strut. The mass properties evaluated were the total mass, the longitudinal axis center of gravity, and the moment of inertia about one of the transverse axes. The results are summarized in Table IV-1 below which shows that both of the computer models match the sample strut to within five percent. In regard to the mass measurement, the lower values for the models were expected because the synthetic rubber coating and lug protrusions were not included. The detailed procedure used to determine the measured properties is included in Appendix A.

Property	Measured	AutoCAD		NASTRAN	
		Computed	Percent Difference	Computed	Percent Difference
Total Mass (lbm)	28.61	26.97	-5.73	27.21	-4.89
Center of Gravity (in)	13.38	13.49	0.82	13.46	0.60
Moment of Inertia ($lbm\text{-}in^2$)	4027	3935	-2.28	3986	-1.02

Table IV-1. Drag Strut Mass Properties Comparison

D. MODELING OF EQUIVALENT SPHERICAL PITS

The results of the corrosion attribute measurement described in Appendix A were used to create a model that included all of the grid element pitting. A cut-away view of half of the cylindrical portion of that model is shown in Figure IV-2 below. The pit modeling was performed in AutoCAD as described in Appendix C. The pitting configuration could not be modeled with finite elements with less than 5,000 nodes due to the level of geometric complexity.

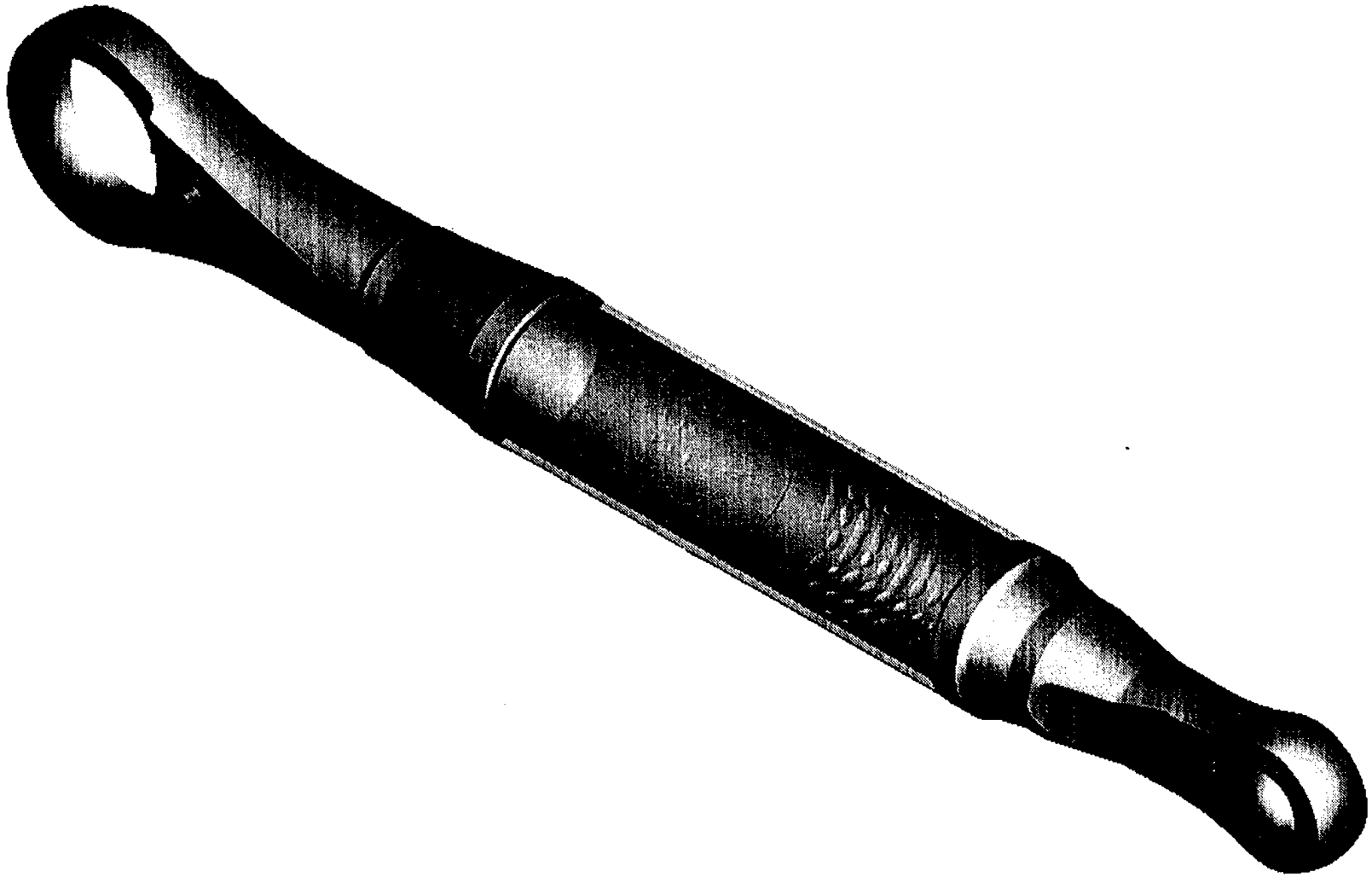

Figure IV-2. AutoCAD Model Including Grid Element Spherical Pitting.

V. DRAG STRUT BUCKLING ANALYSIS RESULTS

A total of 34 drag strut configurations were modeled and analyzed using both AutoCAD and MSC/NASTRAN for Windows. These configurations ranged from the nominal strut, with no corrosion effects, to struts with several two inch holes through them. The analyses included the linear static compression case and two to three linear buckling cases. In addition, several linear static tension cases were performed to uncover any peculiarities between compression and tension. As discussed above, the load boundary conditions in tension caused an incorrect stress concentration in the lugs; however the far field stress was correct. The conclusion was that the highest stress element and value matched the compression case and thus tension analyses for all the configurations was unnecessary. The following sections contain a brief description of each configuration, along with a diagram and the buckling and yield load data. All of the load data is in thousands of pounds or kilo-pounds (kips). The nominal case was used to normalize the remaining load data to highlight the impact of the defects more than the absolute significance of the buckling load itself. Therefore all of the other configuration buckling load data is presented as a fraction of the nominal.

A. NOMINAL CASE

The solid geometry created in AutoCAD was imported into NASTRAN and meshed with finite elements to produce the nominal strut without corrosion effects. Two models were produced from this configuration with different maximum element sizes. The first had an element size of 0.415 inches which resulted in 4,990 total nodes and 14,723 elements. This was below the 5,000 node limit but left no room for growth. Another model was built with an element size of 0.420 inches, resulting in 4,829 nodes and 14,247 elements. This became the standard element size for all future models to assure some consistency in results. The result of a buckling analysis on the nominal model, including the deformed shape after buckling and colored Von Mises stress contours, is shown in Figure V-1.

Figure V-1. Nominal Drag Strut MSC/NASTRAN Elastic Buckling Analysis Results.

A model number was assigned for configuration identification among all 34 configurations analyzed. The model number is included with each subsequent strut image for identification. The buckling analysis on the nominal strut also provided the locations for the critical nodes for the first three buckling mode shapes. These locations were then used to locate pits and other defects in future configurations. The first three buckling mode shapes and the locations for the critical nodes are indicated by the arrows in Figure V-2 below.

1. First Buckling Mode

Buckling Load: P_{cr} = 729.0

Node Location: x = 15.083
y = 0.000
z = 1.888

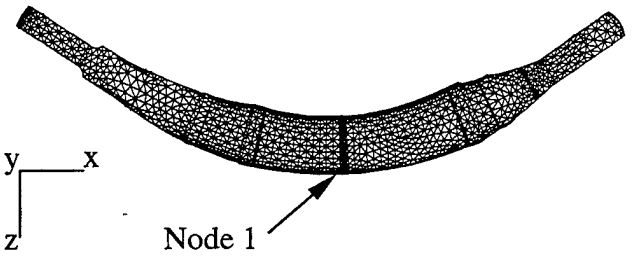

2. Second Buckling Mode

Buckling Load: P_{cr} = 760.6

Node Location: x = 16.008
y = -1.888
z = 0.000

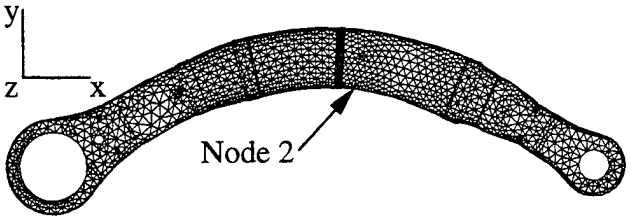

3. Third Buckling Mode

Buckling Load: P_{cr} = 2,215

Node Location: x = 5.598
y = 0.000
z = 1.500

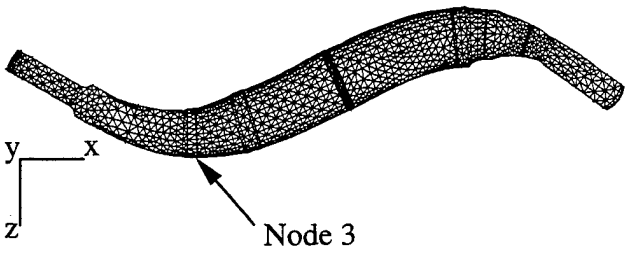

Figure V-2. First Three Buckling Modes (Units: Loads - kips., Locations - in.)

B. SIX MOST SEVERE PITS

The goal of this investigation was to perform an analysis of the lower tail of the probability distribution of the population of all struts. Analyzing the worst case would

provide an upper bound for the risk of today's strut. The limitations discussed above prevented analysis of a model that included all of the corrosion discovered in the sample strut. However a limited model was analyzed with the six most severe pits from the sample strut. Two models were constructed with two different maximum element sizes. The added complexity of the pits forced maximum element sizes of 0.430 and 0.423 respectively. Figure V-3 shows the position of the pits and Table V-1 shows the load data.

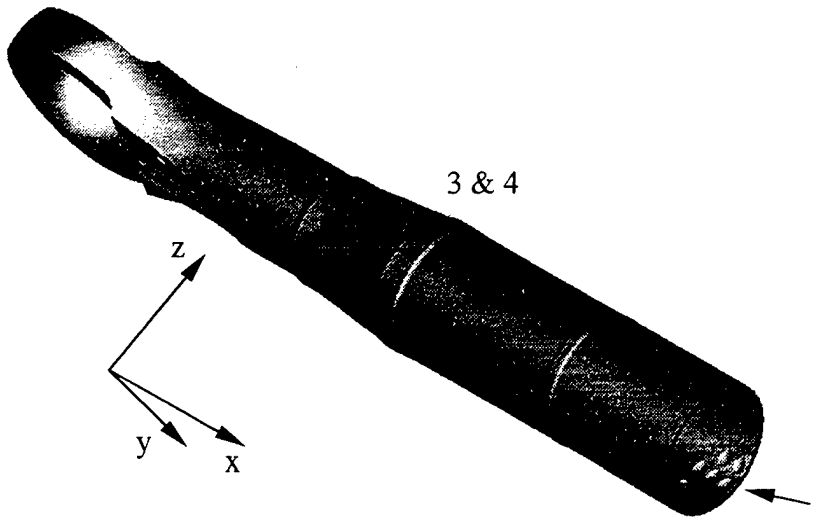

Figure V-3. Six Most Severe Pits.

Model Number	Element Size (in)	Yield Load (kips)	Normalized Buckling Load
3	0.430	298.1	0.995
4	0.423	295.5	0.994

Table V-1. Six Most Severe Pits Load Data.

C. COMPLETELY THIN SECTION

As an extension of the six most severe pits model, a model was created with an entire sector thinned by the depth of the deepest pit discovered, or 0.041 inches. This configuration approximated the instability in the pitted sample strut, because it results in a model that is quite unbalanced in terms of local centroid and moment of inertia. Since

column buckling is directly related to the stability of the structure, this model was assumed to be as unstable as any pitting that would be found in an operational strut. Figure V-4 shows the orientation of the thinned section with respect to the strut. The compressive yield load was 249.9 kips while the normalized buckling load was 0.964.

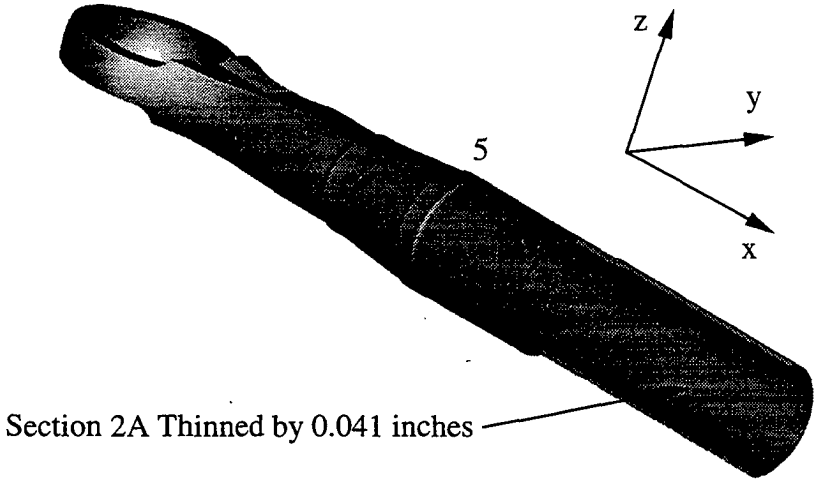

Figure V-4. Completely Thinned Section.

D. MORE SEVERE SPHERICAL PITS

The next step was to find the upper bound of the risk for a strut more corroded than the sample strut. This would represent the strut of the future that is allowed to continue to corrode. In this case the pits were deep enough to extend to the limit of the wall thickness or 0.160 in. In addition, these very severe pits were located at the critical locations determined from the nominal strut. There were seven models created: three configurations of one pit at a single node, three configurations of combinations of two pits at two different nodes, and finally, one configuration of pits at all three nodes. The spherical pit radius was set at twice the pit depth so that the lip of the pit would not be perpendicular to the wall. This was done to match the majority of the pits observed during the sample strut dissection and is explained in more detail in Appendix B. Figure V-5 shows a cutaway drawing of the strut with the three possible pit locations depicted.

Table V-2 shows the various combinations of pits and the associated yield load and normalized buckling load.

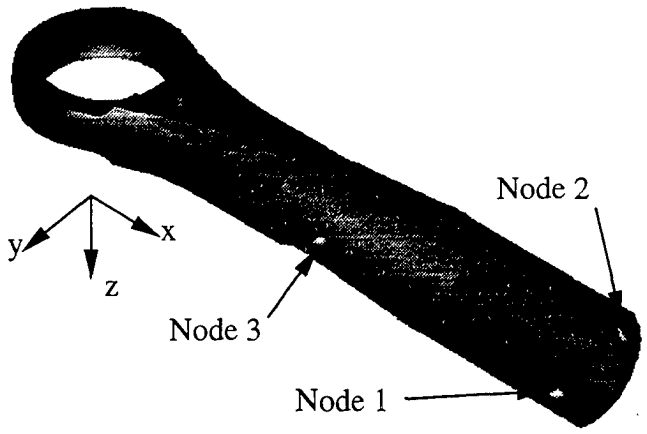

Figure V-5. Spherical Pit Combinations at Nodes 1, 2, & 3.

Model Number	Nodes With Pits	Yield Load (kips)	Normalized Buckling Load
6	1	230.1	0.996
7	2	235.3	0.999
8	3	272.1	0.998
9	1 & 2	230.5	0.997
10	1 & 3	230.0	0.994
11	2 & 3	236.3	0.997
12	1, 2 & 3	229.9	0.994

Table V-2. Spherical Pit Combinations Load Data

E. HOLES AT NODE 1

The results of the more severe spherical pit analysis showed extremely small effect on the buckling load. The next step was to move to more severe configurations that might begin to reveal the point at which pitting could become critical to the buckling failure mode. The spherical pits were replaced with through-the-thickness holes of increasing diameter, from 0.5 to 2.0 inches. This portion of the analysis was confined to node 1 because it is the most critical location. Combinations included holes at node 1, holes on the opposite side of node 1, and holes on both sides at node 1. Figure V-6 shows the various hole configurations and Table V-3 contains the load data.

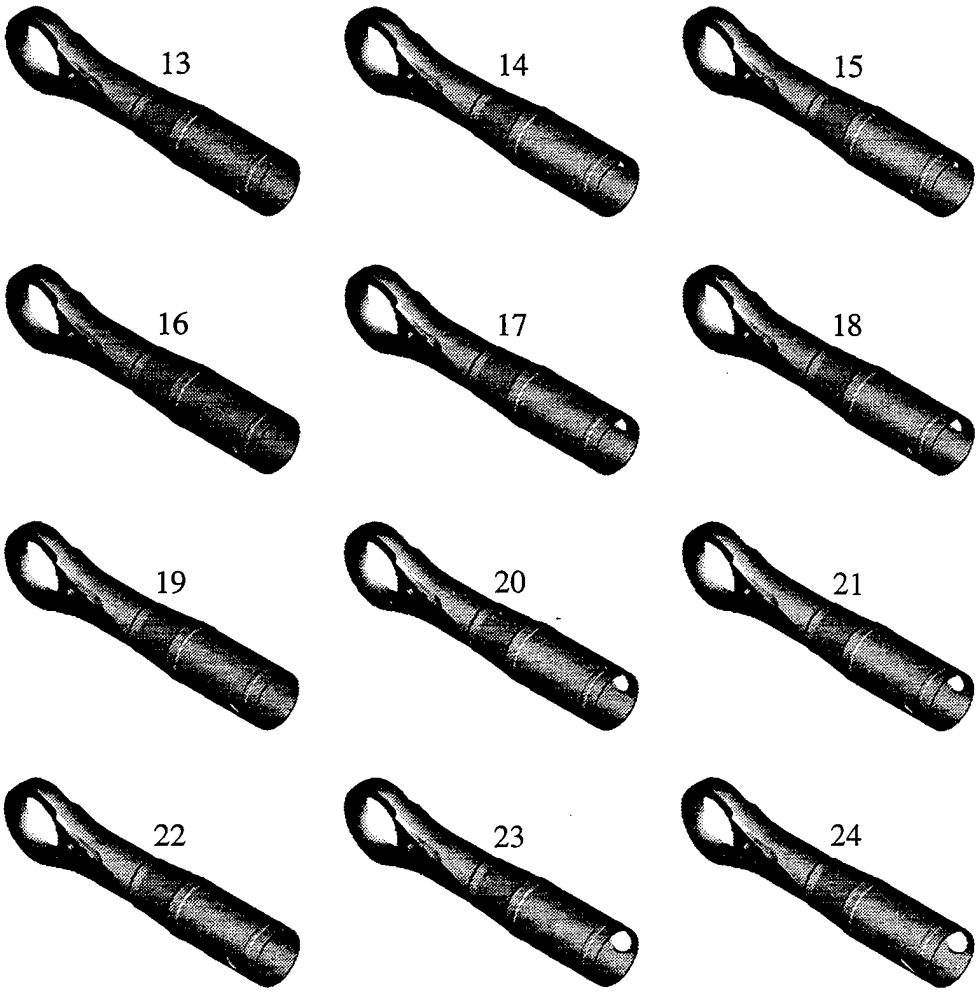

Figure V-6. Hole Combinations at Node 1.

Model Number	Hole Size (in)	Sides With Holes	Yield Load (kips)	Normalized Buckling Load
13	0.5	Front	176.7	0.993
14	0.5	Back	182.7	0.993
15	0.5	Both	182.6	0.989
16	1.0	Front	139.2	0.981
17	1.0	Back	155.1	0.981
18	1.0	Both	145.6	0.961
19	1.5	Front	113.1	0.953
20	1.5	Back	98.8	0.954
21	1.5	Both	95.5	0.911
22	2.0	Front	93.1	0.909
23	2.0	Back	73.4	0.912
24	2.0	Both	64.6	0.822

Table V-3. Node 1 Hole Combinations Load Data

F. HOLES AT NODE 2

To uncover any peculiarities with respect to buckling mode shapes with holes explored above, a similar but less exhaustive approach was applied at node 2. The four configurations analyzed included a single hole at node 2 of diameters from 0.5 to 2.0 inches. As it turned out, a 2.0 inch hole at node 2 had a lower buckling load than the same hole at node 1; however, this was not the case with the yield load. Another peculiarity that the node 2 analysis revealed was that the first buckling mode shape changed when a 1.5 inch or larger hole was present. The shape matched that of the second mode in all prior analysis. Figure V-7 shows the configurations, along with the resulting mode shapes. The load data is presented in Table V-4.

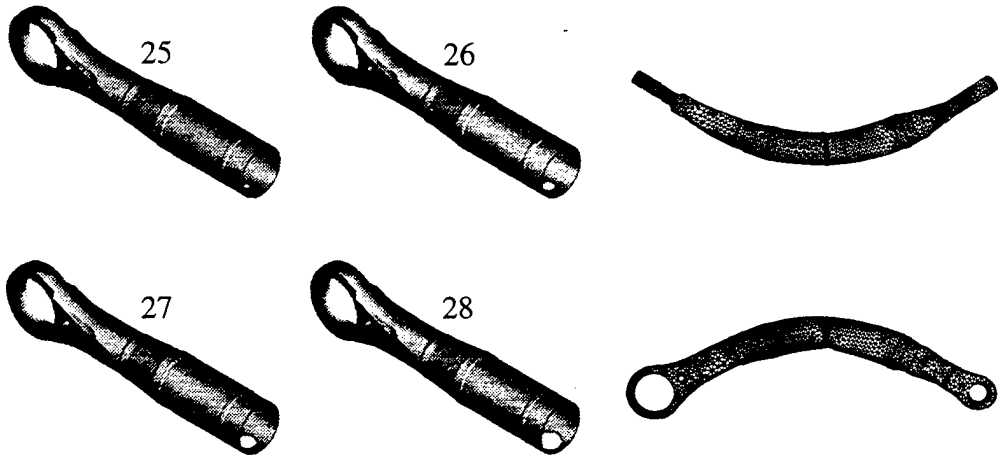

Figure V-7. Holes at Node 2 With Mode Shapes.

Model Number	Hole Size (in)	Yield Load (kips)	Normalized Buckling Load
25	0.5	167.4	0.999
26	1.0	153.9	0.997
27	1.5	110.7	0.990
28	2.0	96.3	0.876

Table V-4. Holes at Node 2 Load Data

G. COMBINATIONS OF HOLES AT NODES 1 & 2

Given the mode shape change observed above, additional combinations of holes at both nodes 1 and 2 were analyzed to study the interaction between the two nodes. In these two cases a 1.5 inch hole was placed at node 2 along with 0.5 and 1.0 inch holes at node 1, respectively. The case with the 0.5 inch hole at node 1 still exhibited the mode shape change observed above; however the 1.0 inch hole forced the first mode shape back to the original case. This demonstrates the dominance of holes (or critical pits) at node 1. Figure V-8 shows the two cases analyzed in addition to the resulting mode shapes. The load data is presented in Table V-4.

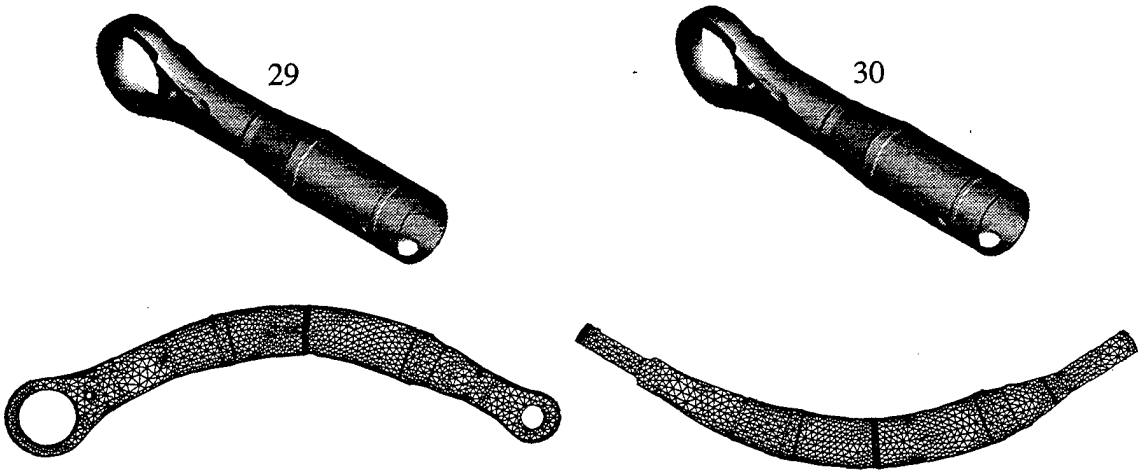

Figure V-8. Hole Combinations at Nodes 1 & 2 With Mode Shapes

Model Number	Hole Size (in)	Yield Load (kips)	Normalized Buckling Load
29	Node 1 - 0.5 Node 2 - 1.5	84.7	0.989
30	Node 1 - 1.0 Node 2 - 1.5	86.4	0.978

Table V-5. Hole Combinations at Nodes 1 & 2 Load Data

H. OTHER HOLE COMBINATIONS

All the preceding configurations contained pits or holes only at critical nodes. To verify that those cases are the worst case and to study the effect of clustering holes

around one location, the following configurations were analyzed. The first was a 0.5 inch hole three inches closer to the end of the strut than node 1 (x = 12 inches). The expectation was that this would yield a higher buckling load than the case of the same hole at node 1. The results yielded a normalized buckling load of 0.997, which is higher than the value of 0.993 found model number 10 above. The other cases analyzed included clustering of three 0.5 inch holes around node 1. In one case the holes were spaced 1.0 inches apart, along the x axis. In the other two cases, the holes were arranged 20 and 40 degrees apart, respectively, around the circumference at node 1. All four of these cases are shown in Figure V-9. The load data is presented in Table V-6.

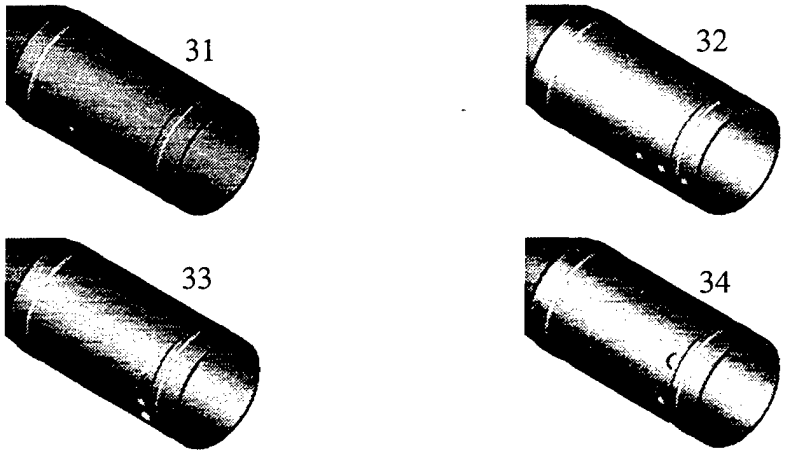

Figure V-9. Other Hole Combinations.

Model Number	Hole Size (in)	Hole Location	Yield Load (kips)	Normalized Buckling Load
31	0.5	x = 12 in.	180.7	0.997
32	0.5	Node 1 1 in. Apart	195.6	0.984
33	0.5	Node 1 20° Apart	120.1	0.985
34	0.5	Node 1 40° Apart	180.7	0.989

Table V-6. Other Hole Combinations Load Data.

I. BUCKLING ANALYSIS SUMMARY

The result of all the finite element modeling and analysis is the effect of corrosion on the buckling strength of the strut in terms of normalized buckling load. The conclusion is that even severe corrosion, much more severe than would ever be accepted in operational use, has minimal impact on the buckling strength. This is highlighted in Table V-7 which is a listing of all the strut configurations modeled, sorted by corrosion severity.

Finite Element Analysis Results																		
4340 Steel Yield Stress (psi) = 200000							Compressive Yield			Buckling								
										Mode 1				Mode 2				Notes
Number	Model #	Prob. Of Severity P(S)	Prob. Of Location P(L)	Joint Prob. Of Occur. P(S)*P(L)	Total Nodes	Total Elements	Element Number	Max Stress (psi)	Yield Load (kips)	Buckling Load (kips)	Normal Buckling Load	Element Number	Max Stress (ksi)	Buckling Load (kips)	Normal Buckling Load	Element Number	Max Stress (ksi)	(MS = Modes 1 & 2 swap order)
0	1	N/A	N/A	N/A	4990	14743	11730	0.774	258.6	724.5	N/A	7729	435.8	755.5	N/A	8497	452.5	Nominal, no pitting, eccentric
1	2	N/A	N/A	N/A	4829	14247	11260	0.744	268.7	729.0	1.000	7400	433.5	760.6	1.000	8126	455.7	Nominal, no pitting, eccentric
2	25	1.20E-07	2.31E-03	2.77E-10	4822	14222	8233	1.195	167.4	728.5	0.999	8137	449.9	755.7	0.994	8233	910.9	0.5 hole at node 2
3	7	3.00E-07	2.31E-03	6.94E-10	4830	14249	8130	0.850	235.3	728.4	0.999	7398	431.8	758.2	0.997	8130	646.8	0.318 pit at node 2
4	8	3.00E-07	2.31E-03	6.94E-10	4877	14385	11372	0.735	272.1	727.6	0.998	3334	468.2	760.7	1.000	8240	456.5	0.318 pit at node 3
5	31	1.20E-07	2.31E-03	2.77E-10	4753	13997	5955	1.107	180.7	727.2	0.997	7164	443.6	758.0	0.997	5890	783.5	0.5 hole at x=12 in -xy plane
6	11	6.26E-08	5.36E-06	3.35E-13	4876	14363	8247	0.846	236.3	727.0	0.997	3324	464.3	758.0	0.997	8247	645.2	0.318 pit at nodes 2 & 3
7	9	6.26E-08	5.36E-06	3.35E-13	4863	14339	7490	0.868	230.5	726.7	0.997	7490	624.7	758.3	0.997	8241	646.7	0.318 pit at nodes 1 & 2
8	26	5.21E-09	2.31E-03	1.21E-11	4746	13987	7846	1.299	153.9	726.7	0.997	7124	433.0	744.1	0.978	7846	969.0	1.0 hole at node 2
9	6	3.00E-07	2.31E-03	6.94E-10	4858	14331	7462	0.869	230.1	726.4	0.996	7462	628.2	760.6	1.000	8206	455.2	0.318 pit at node 1
10	3	3.77E-05	1.54E-16	5.81E-21	4790	14066	11050	0.671	298.1	725.6	0.995	6817	429.5	757.9	0.996	6807	445.5	6 worst pits (Sect 2A)
11	10	6.26E-08	5.36E-06	3.35E-13	4917	14523	7594	0.869	230.0	724.9	0.994	7594	626.6	760.5	1.000	8398	451.6	0.318 pit at nodes 1 & 3
12	4	3.77E-05	1.54E-16	5.81E-21	4941	14526	11426	0.677	295.5	724.5	0.994	7859	436.2	755.8	0.994	7891	454.3	6 worst pits, smaller element
13	12	2.5[illegible]	1.24E-08	3.11E-16	4920	14520	7612	0.870	229.9	724.5	0.994	7612	625.0	757.8	0.996	8371	646.5	0.318 pit at nodes 1, 2, & 3
14	13	1.20E-07	2.31E-03	2.77E-10	4871	14385	7423	1.132	176.7	724.1	0.993	7423	774.8	758.7	0.998	8231	455.3	0.5 hole at node 1
15	14	1.20E-07	2.31E-03	2.77E-10	4872	14378	7430	1.094	182.7	723.9	0.993	7430	742.3	758.5	0.997	7437	451.8	0.5 hole opposite node 1
16	27	8.34E-10	2.31E-03	1.93E-12	4706	13821	7752	1.806	110.7	722.0	0.990	7752	1265.2	726.3	0.955	7752	473.2	1.5 hole at node 2 (MS)
17	29	6.57E-10	5.36E-06	3.52E-15	4803	14111	8025	2.361	84.7	720.8	0.989	8025	1722.2	723.6	0.951	8025	880.1	0.5/1.5 hole node 1/2 (MS)
18	34	9.98E-09	1.24E-08	1.24E-16	4871	14356	7425	1.107	180.7	720.8	0.989	7407	782.3	755.8	0.994	7423	542.9	3 0.5 holes 40° apart node 1
19	15	2.50E-08	5.36E-06	1.34E-13	4946	14567	7620	1.096	182.6	720.7	0.989	7620	743.9	757.6	0.996	7653	462.9	0.5 hole both sides node 1
20	33	9.98E-09	1.24E-08	1.24E-16	4856	14312	7429	1.665	120.1	717.8	0.985	7434	1121.4	756.9	0.995	8211	456.4	3 0.5 holes 20° apart node 1
21	32	9.98E-09	1.24E-08	1.24E-16	4956	14557	6874	1.023	195.6	717.1	0.984	6852	677.2	755.9	0.994	8240	451.2	3 0.5 holes 1.0 apart node 1
22	16	5.21E-09	2.31E-03	1.21E-11	4830	14241	7357	1.436	139.2	715.5	0.981	7357	1086.8	757.7	0.996	8161	451.8	1.0 hole at node 1
23	17	5.21E-09	2.31E-03	1.21E-11	4841	14267	7439	1.289	155.1	715.3	0.981	7439	895.2	757.7	0.996	8229	457.3	1.0 hole opposite node 1
24	30	3.63E-10	5.36E-06	1.95E-15	4759	13948	7867	2.314	86.4	713.2	0.978	7151	1057.7	720.1	0.947	7867	1766.4	1.0/1.5 hole node 1/2
25	5	3.50E-10	2.31E-03	8.09E-13	4878	14418	8161	0.800	249.9	702.6	0.964	8316	452.6	727.2	0.956	8658	512.8	Sector 2A thinned by 0.041"
26	18	1.09E-09	5.36E-06	5.83E-15	4831	14181	7278	1.373	145.6	700.7	0.961	7278	967.9	753.8	0.991	6656	455.7	1.0 hole both sides node 1
27	20	8.34E-10	2.31E-03	1.93E-12	4772	14062	7707	2.024	98.8	695.8	0.954	7707	1458.6	759.1	0.998	7946	455.3	1.5 hole opposite node 1
28	19	8.34E-10	2.31E-03	1.93E-12	4755	13983	7172	1.769	113.1	694.6	0.953	7172	1214.5	758.9	0.998	7136	456.4	1.5 hole at node 1
29	23	2.27E-10	2.31E-03	5.26E-13	4736	13914	7356	2.726	73.4	664.7	0.912	7356	1570.5	757.6	0.996	7655	479.5	2.0 hole opposite node 1
30	21	1.74E-10	5.36E-06	9.33E-16	4734	13926	7089	2.093	95.5	664.2	0.911	7089	1656.4	757.3	0.996	7031	457.5	1.5 hole both sides node 1
31	22	2.27E-10	2.31E-03	5.26E-13	4722	13880	7107	2.149	93.1	662.8	0.909	7107	1318.8	757.0	0.995	7107	450.1	2.0 hole at node 1
32	28	2.27E-10	2.31E-03	5.26E-13	4681	13724	7811	2.077	96.3	638.9	0.876	7811	1332.1	722.4	0.950	7409	458.0	2.0 hole at node 2 (MS)
33	24	4.74E-11	5.36E-06	2.54E-16	4613	13479	7054	3.094	64.6	599.2	0.822	7054	1706.4	752.7	0.990	7054	480.5	2.0 hole both sides node 1

Table V-7. Summary of Drag Strut Finite Element Analysis Results.

VI. RISK ASSESSMENT FROM A SINGLE RANDOM VARIABLE

The risk assessment for the drag strut in the presence of corrosion was made by dividing the problem into two distinct modes. The buckling risk assessment was performed by comparing the probability of occurrence of corrosive severity, mapped into buckling load, to the operational service load. The yield and fracture assessment should be performed by direct filtering with a low temperature proof test.

A. COLUMN BUCKLING RISK ASSESSMENT

Certain significant corrosion configuration buckling loads were determined from finite element analysis as previously described. Each of the 32 cases became data points in a probability distribution in terms of buckling load and the probability of occurrence for the pitting required to create the configuration analyzed. All of the corrosion configurations that could exist in the strut could not possibly be modeled; therefore, a complete probability distribution could not be assembled. However, an estimate of a probability distribution function (PDF) could be fit on top of the 32 data points that were modeled. The relationship of corrosion severity to buckling load is neither linear, monotonic, nor homologous because of the importance of the location of the pitting relative to the critical nodes in the strut. This is demonstrated in Figure VI-1, which shows the 32 corrosion configuration buckling loads and their respective joint probability of occurrence. The assumption was made that the real strut PDF would be in the form of a Weibull distribution because a severe pit in a critical location would be the weak link that would cause the strut to buckle. A Weibull distribution curve fit was performed until a PDF resulted that reasonably encompassed all of the analysis data. The shape and scale parameters for that PDF are shown in Figure VI-1.

With the shape and scale parameters from the PDF, a cumulative distribution function (CDF) could also be plotted as a function of buckling load. The CDF provided the crucial relationship necessary to perform the risk assessment; however one more step was necessary to make the CDF relate to the operation envelope of the drag strut. The buckling loads were determined using a linear-elastic buckling analysis. As expected, the

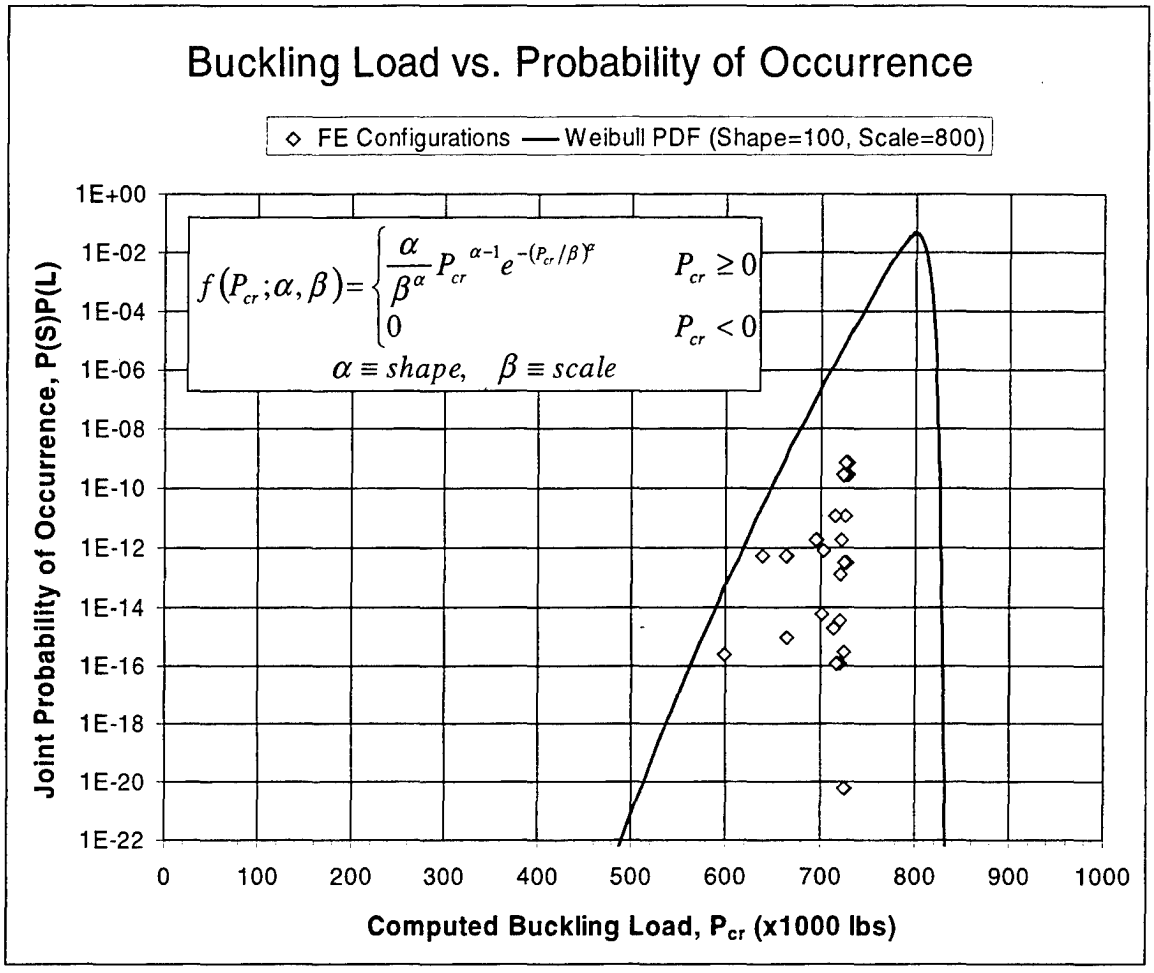

Figure VI-1. Buckling Load PDF Approximation.

values of the computed loads were significantly higher than the design load or the operational load. This indicated that plastic deformation of the strut must occur prior to buckling. The discussion included in Appendix D shows the significance of this phenomenon demonstrated through buckling testing on aluminum tubes that matched the buckling characteristics of the drag strut. The relative impact of corrosion severity on the linear-elastic buckling solutions was assumed to be transformable to the operational and design load regime of the real strut. This transformation was performed by adjusting the scale parameter of the Weibull distribution to that of the manufacturers estimate of the critical buckling load for the nominal drag strut [Ref. 1]. This transformation is shown graphically in Figure VI-2. Included on the figure is the operational envelope of the strut in compression load, displayed at the Man-Safe reliability threshold of one failure out of

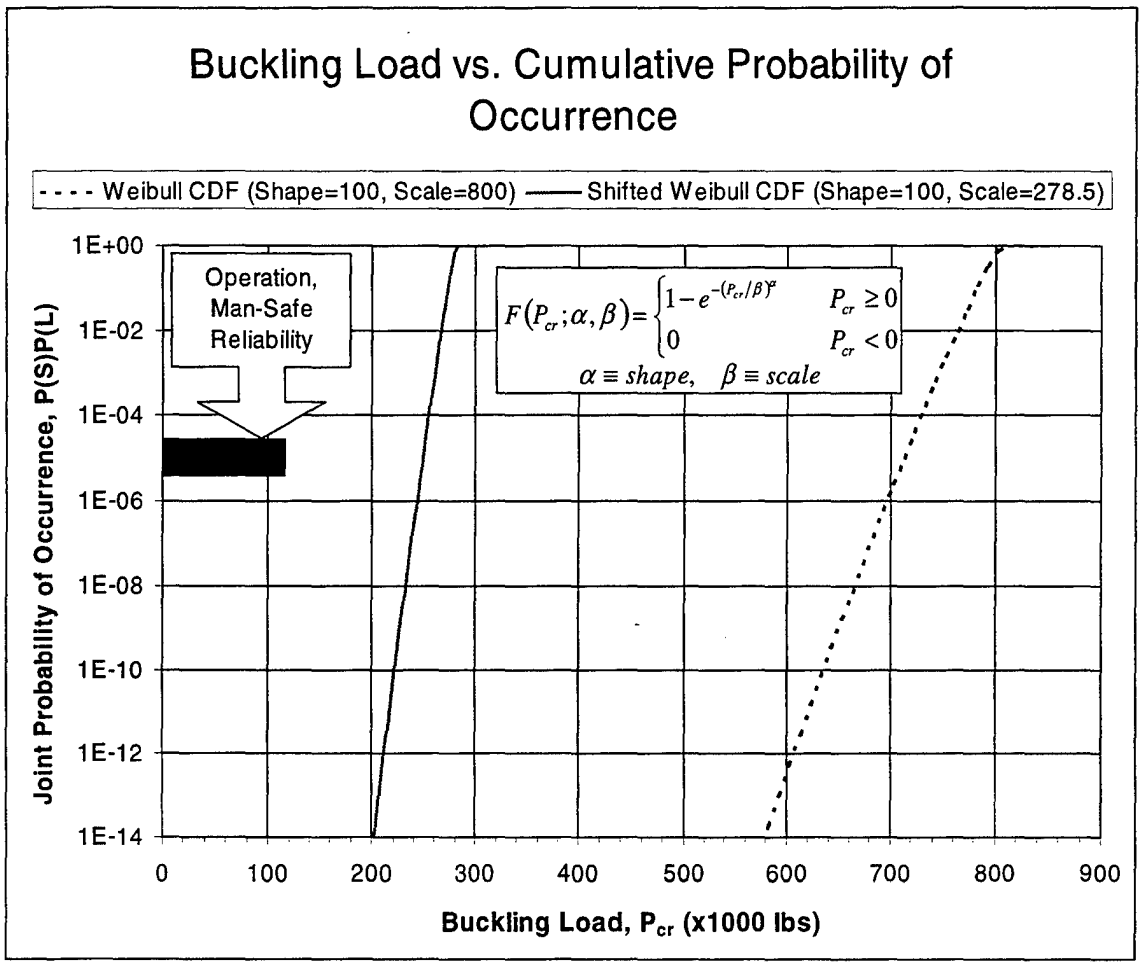

Figure VI-2. Buckling Load CDF Transformation.

100,000 struts, or a probability of occurrence of $1x10^{-5}$. This is the risk assessment for compressive buckling of the strut. The shifted Weibull curve represents the buckling load given the joint probability of occurrence of severe pitting at a critical location. The curve indicates that it is extremely improbable that corrosion will cause buckling in the operational load environment of the drag strut.

B. YIELD AND FRACTURE RISK ASSESSMENT

The risk assessment for yielding or fracture from fatigue could be performed in a traditional manner by conducting statistically significant testing on actual hardware. This method is indirect because it does not assure the reliability of any particular strut, only

the general reliability of the population of struts. In the presence of corrosion, this method is inadequate because one could never achieve statistical significance in the face of the corrosion variability. A direct method for not only assessing the risk, but assuring the reliability of every strut is a low temperature proof test.

The rationale for performing a low temperature proof test comes from estimation of the time-temperature relationship of first order kinetics. Every 10° C decrease in temperature is equivalent to a reduction in time by one half. If, for example, a proof test were performed at a particular load for 100 seconds at a temperature of –200° C it would be equivalent to performing the same test for 0.1 milliseconds at 0° C. This can be seen from:

$$t_{equivalent} = t \cdot 2^{\frac{\Delta T}{10}} = (100)\left(2^{\frac{-200}{10}}\right) = 0.0001 \text{ sec} \qquad (10)$$

This time is too short for any flaw growth to occur; therefore, the proof test does not cause damage to any strut that passes the test. By the same application of the first order kinetics approximation, any flaw that already exists in the strut will cause catastrophic failure. The time shift causes the loading at low temperature to be equivalent to an impact load at normal temperature and the strut behaves as if it were extremely brittle. Therefore there is no time for dislocations to move and no yielding occurs, but a critical flaw causes failure. The result is a direct, high pass filtering of any weak struts, with no damage to the surviving struts. The test could be performed using liquid nitrogen which has a boiling point of –196° C (-320° F) or approximately 216° C below room temperature. Cooling the strut to liquid nitrogen temperatures would provide the necessary time shift as shown above. The low temperature proof test would assure that each tested strut would neither yield nor fracture in fatigue at the operational load.

It would not be necessary to perform both a tension and a compression proof test. Because of the equivalence of the tensile and compressive yield criterion, such as described by Von Mises stress or maximum shear stress, it is only necessary to perform a tensile proof test. If a strut does not yield in tension, then it would not yield in compression either.

To provide an additional level of confidence in the fatigue life of a corroded strut, several struts that have been rejected by current inspection methods could be proof tested at low temperature. The ones that pass could then be fatigue tested, either as a whole strut, or as dog bone coupons. The data from these tests could be used to determine the both the remaining fatigue life and the residual strength of the surviving struts. This information would also indicate the required interval for subsequent proof tests for each specific strut after continued service.

C. COMBINED RISK ASSESSMENT

The two individual risk assessments combine to provide the quantitative assessment necessary to assure corroded strut reliability. The buckling analysis showed the following key points:

1. Severe corrosion at a critical location is highly improbable. The joint probability of occurrence of a severe corrosive pit at a specific location is less than one in a million or $1x10^{-6}$.
2. Column buckling of the strut occurs only after plastic yielding has occurred.
3. The finite element solutions provided very accurate plastic yield load data and the plastic yield loads were always less than the buckling load for the same configuration.
4. A corroded strut would have to yield prior to buckling.
5. The transformed CDF indicates that buckling due to corrosion is extremely improbable.

If a particular strut survives a low temperature proof test, then that strut will not yield at the operational load and therefore it will not buckle. In addition, the strut would not possess a flaw large enough to be critical in terms of flaw growth and fatigue fracture.

VII. CONCLUSIONS

An investigation was performed on the effect of internal corrosion on the buckling strength of P-3C main landing gear lower drag struts. Based upon the results of both the corrosion measurement and probability distribution definition process and the finite element analysis, the probability of a drag strut buckling in operational service was found to be less the one chance in a million, which is extremely remote. Therefore the column buckling failure mode for a severely corroded P-3C main landing gear lower drag strut is not an issue.

A low temperature proof test could be performed that would assure that a specific strut would neither yield nor fracture at the operational load. The tensile yield test would also assure that compressive yielding would not occur because of equivalent yield criterion. Additionally, if the strut would not yield, then it could not buckle either.

The reliability assurance for the drag strut in the presence of corrosion is summarized in Figure VII-1. The operational environment is contained within the filtered domain defined by the low temperature proof test. The hash-marked portion of the compression operating region represents the loading condition that can only result from full braking while taxiing in reverse. Because the fleet operators never perform this operation, the likelihood of the strut buckling is even more improbable. The finite element analysis of buckling load region is separated from the filtered domain by the assurance domain. The size of the assurance domain, although displayed in load, is in terms of probability of occurrence of either corrosion severity or the time required to produce the corrosion.

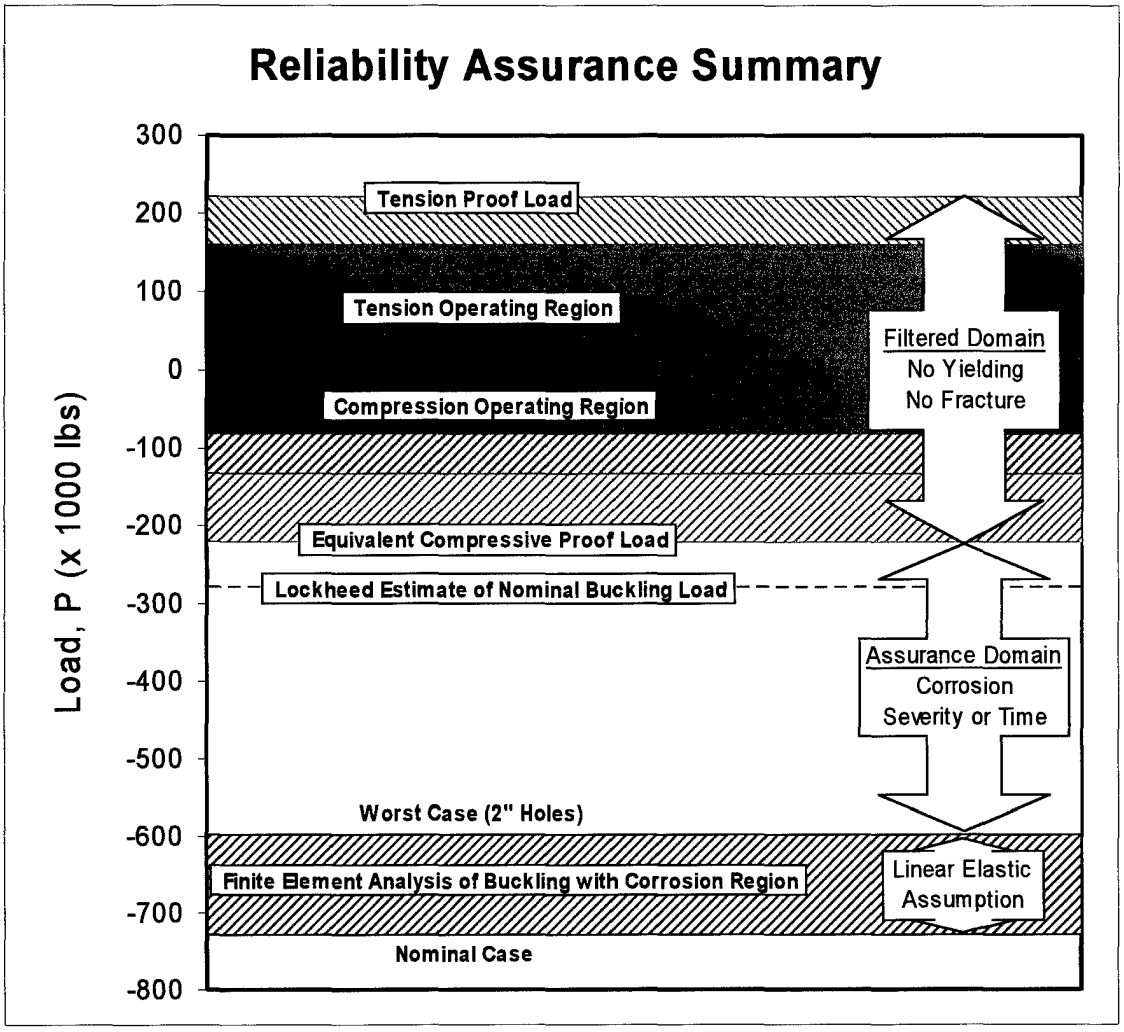

Figure VII-1. Reliability Assurance Summary.

VIII. RECOMMENDATIONS

Based upon the results of this investigation, the following recommendations are provided for the P-3 Class Desk Officer, Program Manager Air, Maritime Surveillance Aircraft (PMA-290):

1. Perform a low temperature proof test on main landing gear lower drag strut currently in service. Place the surviving struts back in service for a length of time commensurate with the confidence level of the fatigue life remaining. Determination of that fatigue life was beyond the scope of this investigation.

2. Develop a method to prevent further corrosion by either sealing the internal cavity of the strut and filling it with an inert gas, such as nitrogen, or coating the internal surface with a corrosion inhibitor. Other possibilities include placing some kind of organic or inorganic desiccant in the cavity to remove the moisture that provides the corrosive environment. The analysis in this investigation suggests that continued corrosion may still be acceptable in terms of buckling because of the extremely improbable effect of corrosion on buckling load. However, the effect of continued corrosion upon the fatigue life of the strut was beyond the scope of this investigation.

3. Perform a low temperature proof test on several previously rejected drag struts. Use the surviving struts for both fatigue life testing, either at the coupon level or as a whole strut, and then residual strength testing to determine the service life remaining as discussed above.

LIST OF REFERENCES

1. Lockheed Aircraft Corporation, California Division, *Main Landing Gear Analysis*, Report No. 13680, 1961.

2. Naval Air Systems Command, *Depot Maintenance With Illustrated Parts Breakdown, Maintenance, Lower Drag Strut Assembly, Part Number 901676-1*, NAVAIR 03-25EK-13, 1994.

3. Lockheed Aeronautical Systems Company, *P-3 Aircraft, Lower Drag Strut LASC-B P/N 901676-1 Inside Corrosion, Engineering Investigation WC1-EI-P3-0170-8R*, Letter Serial No. GLC/88-62995.1, 1988

4. Lockheed Aircraft Corporation, California Division, *Proof Tests of Flashwelded and Unwelded Parts*, Report No. 13682, 1959.

5. MacNeal-Schwendler Corporation, *MSC/NASTRAN for Windows Users Guide*, The MacNeal-Schwendler Corp., 7-3, 1997.

6. Klaus-Jürgen Bathe, *Finite Element Procedures in Engineering Analysis*, p. 165, Prentice-Hall, Inc., Englewood Cliffs, New Jersey, 1982.

7. Lockheed Aircraft Corporation, California Division, *Drag Strut Assembly – Lower, Main Landing Gear*, Drawing No. 901676, 1959.

8. Ana Diaz, "Understanding How Metals Corrode Can Help Build Better Structures", *Corrosioneering*, http://www.clihouston.com/howmetals.htr, September 1998.

9. Walter D. Pilkey, *Formulas for Stress, Strain, and Structural Matrices*, p. 552, John Wiley & Sons, Inc., 1994.

APPENDIX A. REJECTED DRAG STRUT PROCESSING

1. MASS PROPERTIES

a. Total Mass

The mass of the sample drag strut was determined by direct measurement on a digital scale with automatic zeroing capability. The mass was determined to be 28.61 ± 0.01 pounds.

b. Center of Gravity

The center of gravity along the longitudinal (x) axis was measured by first marking the strut using the computed value from the AutoCAD solid model. Then the strut was suspended with fine steel wire around the cylindrical portion at that location, as shown in Figure A-1. The position of the wire was then adjusted in the x-direction until the strut hung with the longitudinal axis in a level attitude. The new wire position was marked and then measured relative to original computed position. The x-axis center of gravity was measured at 13.38 inches from the origin, which is the center of the small hole directly next to the large lug end.

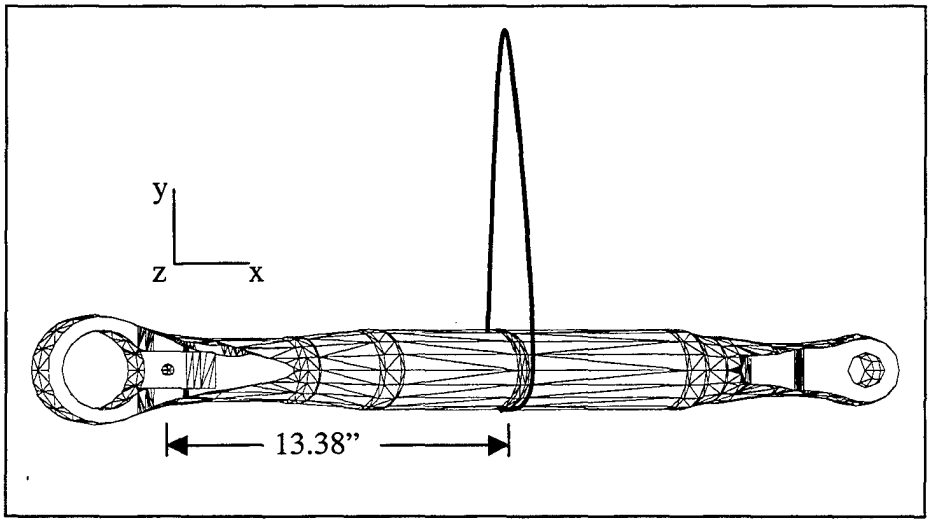

Figure A-1. Center of Gravity Measurement.

c. Moment of Inertia

The moment of inertia about the transverse (z) axis was measured by setting up a compound pendulum problem with the strut suspended from a single, nearly frictionless, pivot point. The strut was supported by stainless steel wire tied around the lug ends as shown in Figure A-2. The strut was hung so that the longitudinal axis was level with the pendulum arrangement at rest. The center of gravity position was verified once again by observing that it was directly below the pivot point. The strut was given a series of gentle pushes until it was observed to swing in a steady arc with rotation purely about the z axis. The period of oscillation was determined by noting the time required for the strut to complete 30 complete oscillations. This timing process was accomplished a twice to verify accuracy. The entire experiment was repeated a second time with the strut suspended at a different pendulum length.

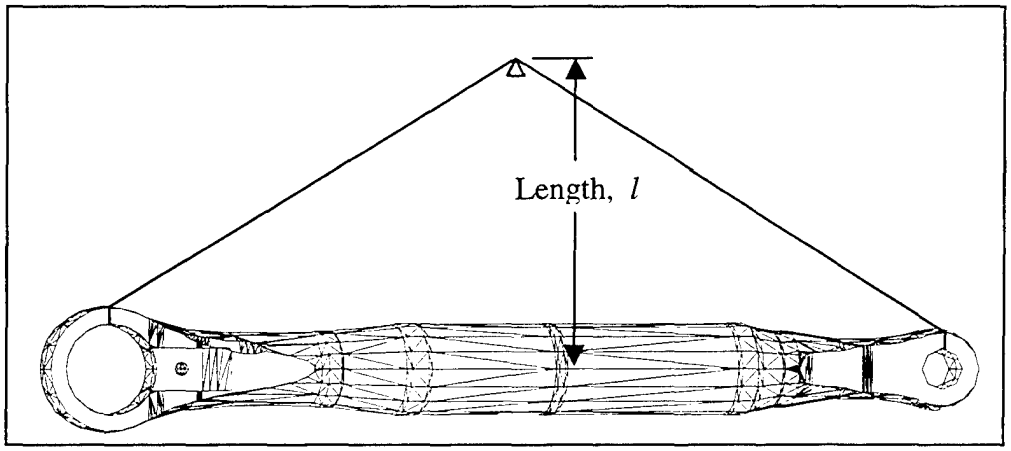

Figure A-2. Compound Pendulum Setup.

Once the period of oscillation was found for the particular setup, the moment of inertia about the center of gravity was calculated from the following relationship:

$$I_{cg} = wl\left[\frac{T^2}{4\pi^2} - \frac{l}{g}\right]$$

where I_{cg} is the strut moment of inertia about its center of gravity, w is the weight of the strut, l is the length from the pivot to the center of gravity, T is the period of oscillation, and g is the acceleration due to gravity. This formula is derived from the

relationship between the period of oscillation and the pendulum length for a simple pendulum and the parallel axis theorem for transformation of moments of inertia about one location to another location. The mass and moment of inertia of the wire were neglected due to their insignificant contribution compared to the mass of the strut.

d. Calculations

The following MATLAB script file was used to calculate the moment of inertia from the collected data:

```
% moment_i.m
% Calculate the moment of inertia of an object about its own
% c.g. given the period of a compound pendulum test.

format compact; clear all;

r = [12.64;12.64;33.06;33.06];  % distance from pivot to c.g. (in)
w = 28.61;   % wieght of the body (lbs)
t = [46.95;46.86;58.64;58.49];  % time for 30 oscillations (sec)
g = 32.174; % acceleration of gravity (ft/sec^2)

T = t/30;  % Period of oscillation (sec)
Icg = w*(r/12).*(T.^2/(4*pi^2)-(r/12)/g); % (slug-ft^2)
Icg_lbm = Icg*g*144; % (lbm-in^2)

disp(' ')
disp('Period of oscillation in seconds')
disp(T)
disp(' ')
disp('Moment of inertia in slug-ft^2')
disp(Icg)
disp(' ')
disp('Moment of inertia in lbm-in^2')
disp(Icg_lbm)
```

The following text is the output from the moment of inertia script file:

```
% OUTPUT %
%» moment_i
%
%Period of oscillation in seconds
%    1.5650
%    1.5620
%    1.9547
%    1.9497
%
%Moment of inertia in slug-ft^2
%    0.8830
%    0.8758
%    0.8785
```

```
%    0.8395
%
%Moment of inertia in lbm-in^2
%  1.0e+003 *
%    4.0910
%    4.0579
%    4.0700
%    3.8894
%»
```

2. DISSECTION, CORROSION REMOVAL, AND MARKING

Once the mass properties were determined, the strut was dissected into sections to allow inspection, corrosion removal, and marking of the grid elements. The strut was first cut across the diameter into five pieces: the two tapered lug ends, the two cylindrical mid-sections, and the center area containing the flash weld. The two cylindrical mid-sections were then cut in half, lengthwise, to allow access to the internal wall surface. The resulting four semi-cylindrical pieces contained the sections of interest for the buckling investigation because the material in these sections carry the bending stress when the strut is put in compression. The remainder of this discussion refers to these four sections. Figure A-3 shows the results of the dissection.

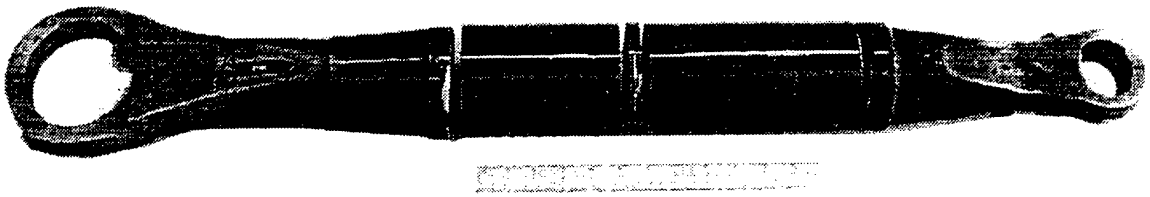

Figure A-3. Drag Strut Following Dissection.

There were large layers of scale that easily flaked off the surface upon initial inspection. Some of this scale is shown in Figure A-4 below. These layers were most likely a combination of excess material from the flash weld process and the synthetic rubber coating that had been hardened by the baking process. The remainder of the corrosion was removed by a combination of mechanical scraping and glass bead blasting. It did not appear that the blasting process affected the base metal because the fine machining marks from initial manufacture were still visible. Finally, the sections were

scribed with grid markings at one half inch by 20 degree intervals. Figure A-5 shows an example of a clean semi-cylindrical section with the grid elements scribed in the surface.

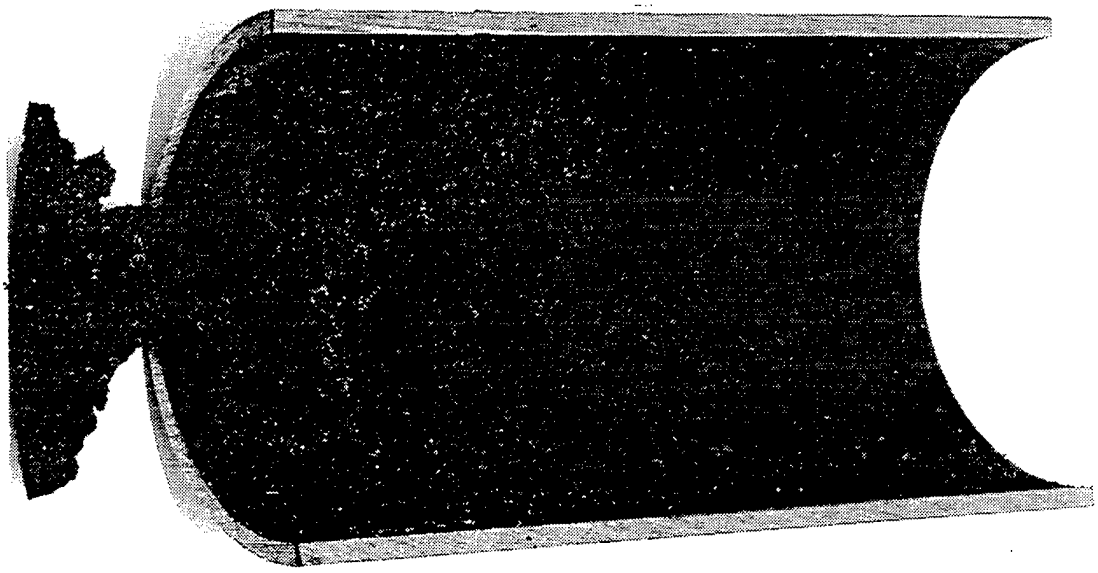

Figure A-4. Semi-Cylindrical Section With Flaking Scale.

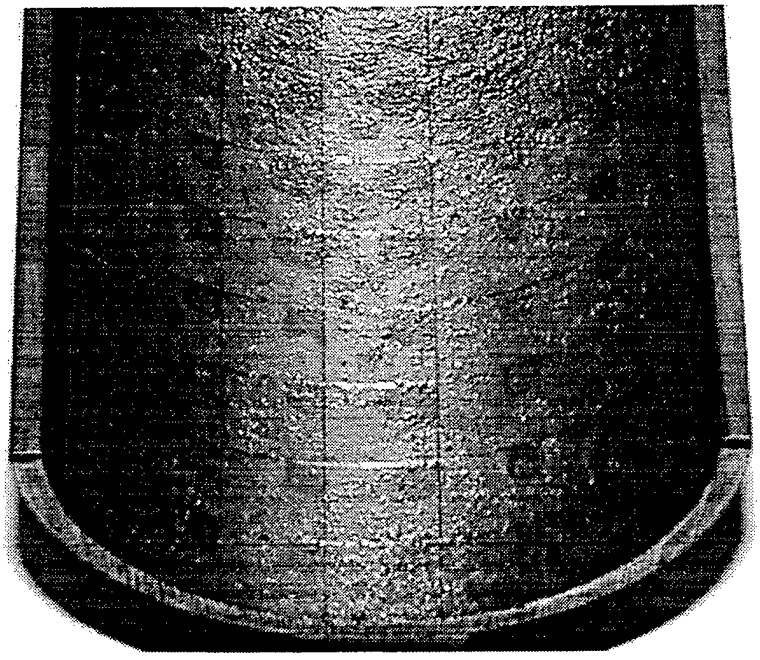

Figure A-5. Semi-Cylindrical Section With Scribed Grid.

3. CORROSION EFFECTS QUANTIFICATION

Once the corrosion was removed from the strut and grid established, the effects of the corrosion process were quantified as follows:

a. Pit Depth

A dial gage capable of measuring linear displacement to 0.001 inches was mounted in a fashion that allowed direct measurement of the section wall thickness and pit depth. The dial gage was fitted with a sharp point that allowed penetration into the narrowest pits. The deepest pit in each grid element was measured and recorded as shown in Table A-1. The deepest pit was 0.041 inches with a remaining wall thickness of 0.119 inches. Thirty-four of the pits were deep enough that the remaining wall thickness was less than the rejection criteria of 0.140 inches. T wall thickness without corrosion across all four sections varied from 0.165 to 0.154 inches. Figure A-6

Radial Grid Index. Increasing Angle About x-axis From x-z Plane. >>>

Longitudinal Grid Index. Increasing x >>>

	(1B)									Large Diameter Lug									(1A)	
	1	2	3	4	5	6	7	8	9	10	11	12	13	14	15	16	17	18	
1	-	9	10	25	25	8	-	-	-	-	-	-	-	-	-	-	-	-	1
2	-	-	16	32	20	20	10	-	-	-	-	-	-	4	-	-	4	6	2
3	-	8	8	21	25	18	15	16	8	-	-	-	11	4	-	-	-	-	3
4	8	10	8	22	30	22	-	-	-	-	-	-	5	4	5	5	4	-	4
5	-	8	10	20	25	5	4	-	-	-	-	-	-	7	5	5	5	6	5
6	4	12	-	20	18	12	-	-	-	-	-	-	4	7	-	4	-	6	6
7	6	7	-	14	13	6	-	-	-	-	-	4	4	-	-	-	-	-	7
8	-	7	4	5	-	6	-	-	-	-	6	5	7	-	-	-	-	-	8
9	-	-	-	-	-	-	-	-	-	-	-	5	4	-	-	-	-	-	9
10	-	-	-	-	-	-	-	-	-	-	-	-	-	-	-	-	-	-	10
	1	2	3	4	5	6	7	8	9	10	11	12	13	14	15	16	17	18	
11	-	-	-	-	-	-	-	15	-	-	-	-	-	-	-	-	-	-	11
12	-	-	8	8	10	9	11	13	7	10	8	-	-	-	-	-	12	10	12
13	-	9	14	12	9	11	10	11	10	15	12	11	11	8	10	14	23	20	13
14	-	10	17	9	14	15	11	11	10	12	12	11	17	22	23	12	15	12	14
15	14	13	14	15	13	23	10	11	9	10	14	13	22	28	20	22	10	15	15
16	9	24	18	21	19	18	10	5	-	8	8	8	41	32	25	20	10	-	16
17	10	17	17	23	19	22	13	5	-	8	-	15	40	38	31	13	10	-	17
18	12	8	11	17	30	7	-	-	-	-	-	-	17	35	35	15	8	-	18
19	-	9	18	22	20	5	-	-	4	-	-	-	12	19	23	12	-	-	19
20	10	10	-	12	19	-	-	-	-	-	-	-	8	15	14	12	-	-	20
21	-	13	7	22	24	-	-	-	-	-	-	-	-	19	10	8	-	-	21
22	8	10	-	22	15	18	-	-	-	-	-	-	-	10	11	-	-	-	22
23	8	7	-	20	12	17	-	-	-	-	-	-	-	20	13	-	-	-	23
24	-	12	-	12	17	17	-	-	-	-	-	-	-	13	15	-	-	-	24
	1	2	3	4	5	6	7	8	9	10	11	12	13	14	15	16	17	18	
					(2B)					Small Diameter Lug									(2A)	

Table A-1. Grid Element Pit Depth (x 10^{-3} in.).

shows the grid element pit depth as a 3D surface plot. The orientation of the plot is 90° to the right of the table. Figure A-7 shows the pit depth measuring set up.

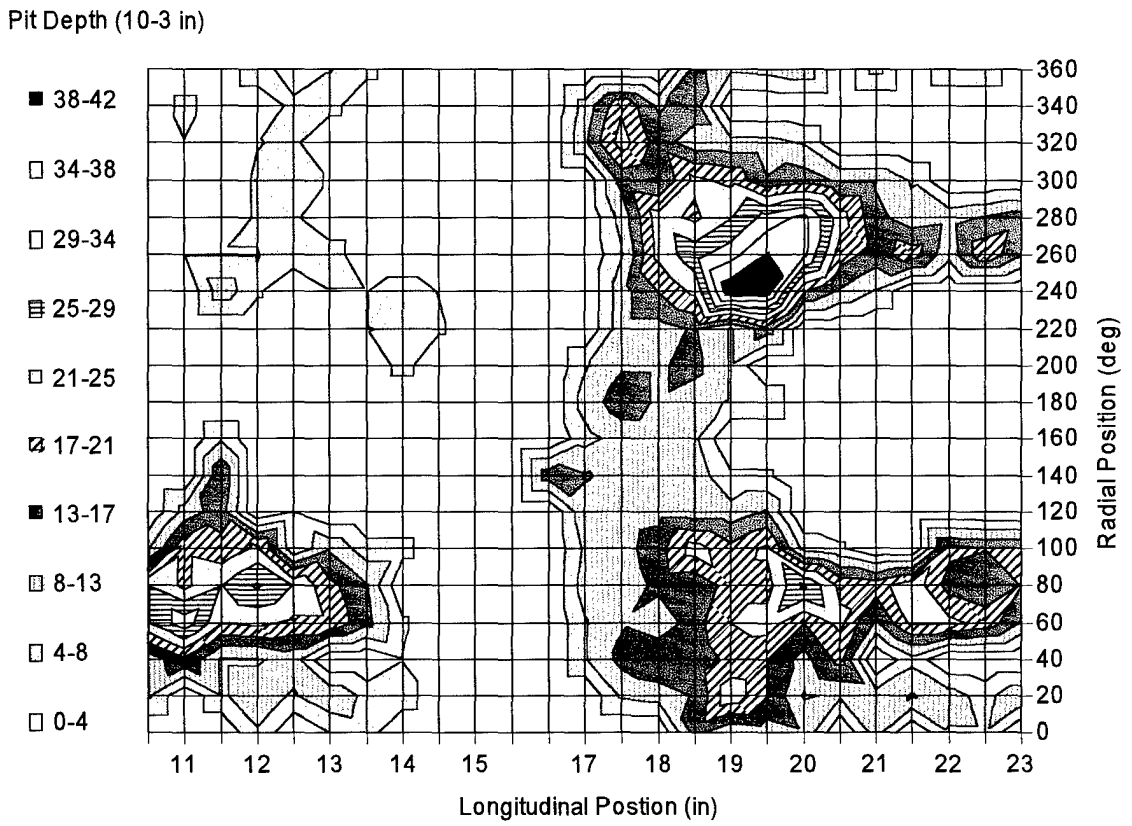

Figure A-6. Strut Corrosion Pit Depth Surface Plot.

b. Pit Volume

The next characteristic of interest was the volume of material removed during the corrosion process. Several measurement schemes were considered including pressing clay into the pits and then measuring the weight of the clay after removing the pieces from each grid element. Then the weight could be converted to volume with the known density of the clay. However, the method of choice was more direct and involved filling the pits in a grid element with a liquid while precisely measuring the volume of liquid required to fill the pits. Alcohol was chosen as the liquid because it spread evenly into the pits and formed a level surface across the top without beading up. A micro-pipette, as

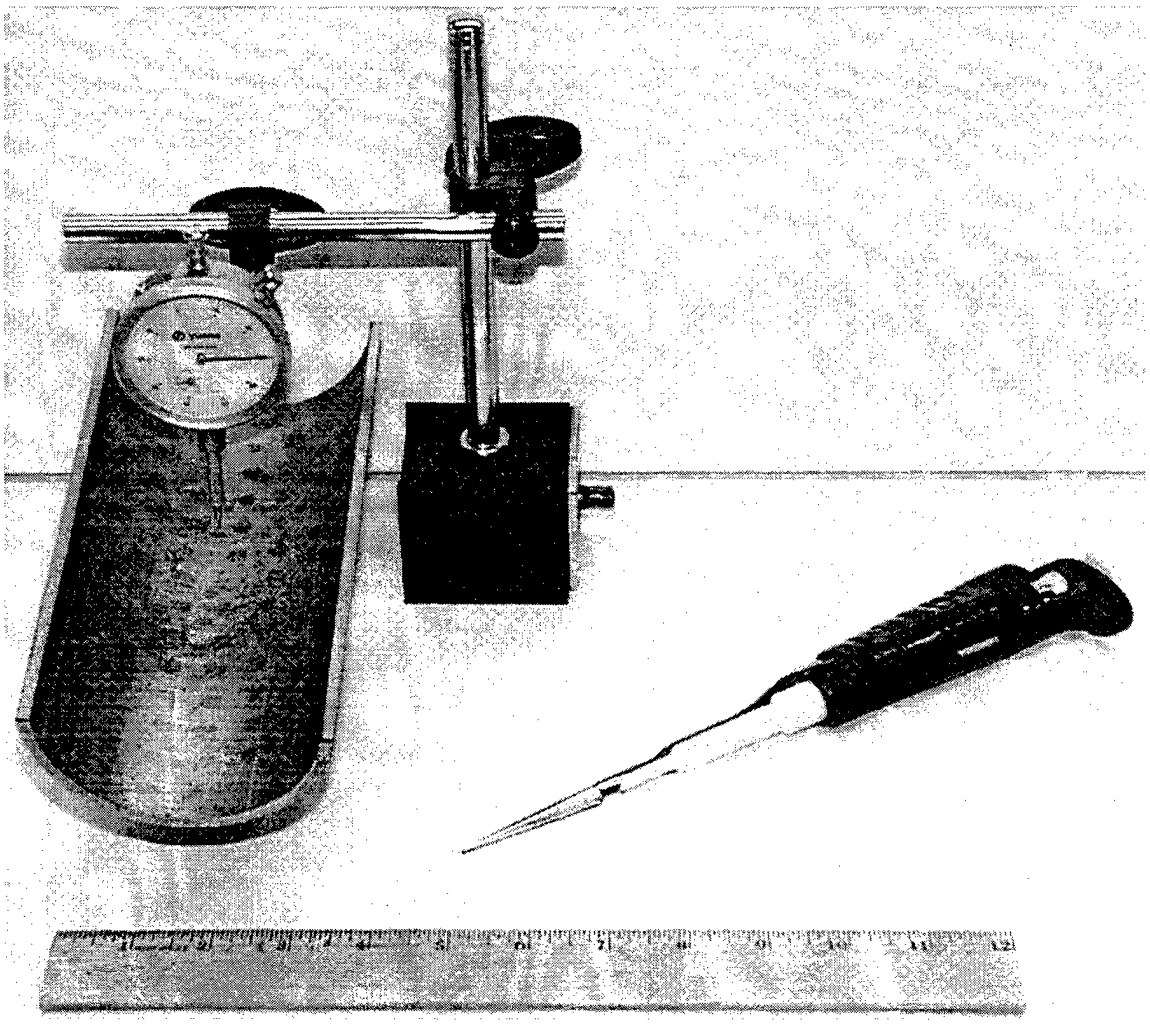

Figure A-7. Pit Depth and Pit Volume Measuring Equipment.

shown in Figure A-7, was used to dispense the alcohol into the pits. This device allowed volume measurement in increments as small as 0.001 milliliters (ml) which corresponds to 6.102×10^{-5} cubic inches (in^3). The largest volume of pits in one grid element was measured to be 0.039 ml. This equates to approximately 300 pieces of 0.5 millimeter (mm) pencil lead or about the size of a kernel of corn. Grid elements with pitting smaller than 0.001 ml were considered to have no pitting at all. The pitting volume in each of the grid elements is presented in Table A-2 below.

Radial Grid Index. Increasing Angle About x-axis From x-z Plane. >>>

(1B) Large Diameter Lug (1A)

	1	2	3	4	5	6	7	8	9	10	11	12	13	14	15	16	17	18	
1	-	1	1	17	9	2	-	-	-	-	-	-	-	-	-	-	-	-	1
2	-	-	3	13	11	18	3	-	-	-	-	-	-	1	-	-	1	1	2
3	-	1	1	12	12	8	5	4	2	-	-	-	1	1	-	-	-	-	3
4	1	1	1	13	12	15	-	-	-	-	-	-	1	1	1	1	1	-	4
5	-	2	2	12	12	2	1	-	-	-	-	-	-	2	1	1	1	1	5
6	1	2	-	10	13	8	-	-	-	-	-	-	1	1	-	1	-	1	6
7	1	1	-	5	7	2	-	-	-	-	-	1	1	-	-	-	-	-	7
8	-	1	1	1	-	1	-	-	-	-	2	2	2	-	-	-	-	-	8
9	-	-	-	-	-	-	-	-	-	-	-	2	1	-	-	-	-	-	9
10	-	-	-	-	-	-	-	-	-	-	-	-	-	-	-	-	-	-	10
	1	2	3	4	5	6	7	8	9	10	11	12	13	14	15	16	17	18	
11	-	-	-	-	-	-	2	3	-	-	-	-	-	-	-	-	-	-	11
12	-	-	4	5	5	4	3	3	2	4	3	-	-	-	-	-	10	8	12
13	-	6	6	6	6	8	4	3	3	8	6	5	4	5	6	10	22	16	13
14	-	7	9	7	7	12	6	4	4	8	8	7	8	13	10	11	16	8	14
15	6	8	12	12	12	14	4	3	2	6	7	8	15	21	18	13	8	5	15
16	5	8	10	14	14	8	4	2	-	4	3	4	20	30	24	15	6	-	16
17	6	8	8	12	12	9	3	1	-	3	-	3	18	39	33	13	8	-	17
18	5	4	3	7	7	4	-	-	-	-	-	-	8	33	29	12	5	-	18
19	-	6	6	8	8	2	-	-	1	-	-	-	5	15	12	7	-	-	19
20	4	6	-	4	4	-	-	-	-	-	-	-	3	10	9	5	-	-	20
21	-	6	3	7	7	-	-	-	-	-	-	-	-	8	7	4	-	-	21
22	3	5	-	9	9	4	-	-	-	-	-	-	-	6	6	-	-	-	22
23	3	2	-	8	8	3	-	-	-	-	-	-	-	5	6	-	-	-	23
24	-	3	-	5	5	3	-	-	-	-	-	-	-	6	3	-	-	-	24
	1	2	3	4	5	6	7	8	9	10	11	12	13	14	15	16	17	18	

Longitudinal Grid Index. Increasing x >>>

(2B) Small Diameter Lug (2A)

Table A-2. Grid Element Pit Volume (x 10^{-3} ml).

c. Equivalent Spherical Pit Radius

Because the exact shape of the pits was not critical to a column buckling analysis there was no attempt made to represent the shape attribute. Instead the depth of the pit and the volume of material missing were chosen as values to be represented. A method was needed to allow proper inclusion of these parameters in AutoCAD and NASTRAN 3D solid geometries. A spherical pit was chosen as a good compromise between modeling ease and the desire to accurately represent as much corrosion effect as possible. The spherical pit size needed to be chosen so that both the pit depth and volume were represented simultaneously. The equivalent spherical pit radius was defined as the radius of a sphere such that a slice from that sphere, at a depth equal to the grid pit depth, would occupy the same volume as the grid pit volume. This is more clearly illustrated in Figure A-8 and is calculated from equation A1 as follows:

$$R = \frac{1}{3}\left(h + \frac{3V}{\pi h^2}\right) \tag{A1}$$

where R is the equivalent spherical pit radius, h is the pit depth, and V is the pit volume. A justification for the choice of this attribute in terms of corrosion pit propagation can be found in Appendix B. The equivalent pit spherical radius values for the grid elements is presented in Table A-3.

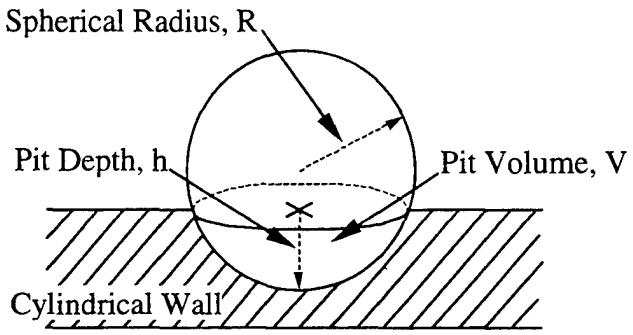

Figure A-8. Equivalent Spherical Pit Radius.

Radial Grid Index. Increasing Angle About x-axis From x-z Plane. >>>

(1B) Large Diameter Lug (1A)

	1	2	3	4	5	6	7	8	9	10	11	12	13	14	15	16	17	18	
1	-	0.243	0.198	0.537	0.288	0.610	-	-	-	-	-	-	-	-	-	-	-	-	1
2	-	-	0.233	0.257	0.541	0.881	0.586	-	-	-	-	-	-	1.215	-	-	1.215	0.542	2
3	-	0.306	0.306	0.536	0.381	0.486	0.437	0.309	0.610	-	-	-	0.164	1.215	-	-	-	-	3
4	0.306	0.198	0.306	0.529	0.269	0.609	-	-	-	-	-	-	0.779	1.215	0.779	0.779	1.215	-	4
5	-	0.610	0.392	0.589	0.381	1.556	1.215	-	-	-	-	-	-	0.795	0.779	0.779	0.779	0.542	5
6	1.215	0.274	-	0.492	0.785	1.083	-	-	-	-	-	-	1.215	0.399	-	1.215	-	0.542	6
7	0.542	0.399	-	0.500	0.809	1.081	-	-	-	-	-	1.215	1.215	-	-	-	-	-	7
8	-	0.399	1.215	0.779	-	0.542	-	-	-	-	1.081	1.556	0.795	-	-	-	-	-	8
9	-	-	-	-	-	-	-	-	-	-	-	1.556	1.215	-	-	-	-	-	9
10	-	-	-	-	-	-	-	-	-	-	-	-	-	-	-	-	-	-	10
	1	2	3	4	5	6	7	8	9	10	11	12	13	14	15	16	17	18	
11	-	-	-	-	-	-	-	0.264	-	-	-	-	-	-	-	-	-	-	11
12	-	-	1.217	1.520	0.975	0.962	0.485	0.349	0.795	0.780	0.913	-	-	-	-	-	1.353	1.557	12
13	-	1.442	0.599	0.813	1.442	1.288	0.780	0.485	0.586	0.696	0.813	0.806	0.646	1.520	1.169	0.996	0.815	0.784	13
14	-	1.363	0.611	1.682	0.698	1.041	0.967	0.646	0.780	1.083	1.083	1.127	0.543	0.529	0.375	1.488	1.386	1.083	14
15	0.599	0.924	1.194	1.041	1.384	0.522	0.780	0.485	0.483	1.169	0.698	0.924	0.609	0.530	0.881	0.529	1.557	0.437	15
16	1.202	0.278	0.606	0.624	0.760	0.486	0.780	1.556	-	1.217	0.913	1.217	0.245	0.580	0.754	0.735	1.169	-	16
17	1.169	0.543	0.543	0.448	0.652	0.369	0.349	0.779	-	0.913	-	0.264	0.232	0.537	0.677	1.499	1.557	-	17
18	0.678	1.217	0.485	0.476	0.161	1.588	-	-	-	-	-	-	0.543	0.535	0.472	1.041	1.520	-	18
19	-	1.442	0.366	0.328	0.395	1.556	-	-	1.215	-	-	-	0.678	0.813	0.448	0.948	-	-	19
20	0.780	1.169	-	0.544	0.222	-	-	-	-	-	-	-	0.913	0.868	0.897	0.678	-	-	20
21	-	0.694	1.192	0.288	0.244	-	-	-	-	-	-	-	-	0.437	1.363	1.217	-	-	21
22	0.913	0.975	-	0.369	0.782	0.246	-	-	-	-	-	-	-	1.169	0.967	-	-	-	22
23	0.913	0.795	-	0.395	1.083	0.207	-	-	-	-	-	-	-	0.249	0.694	-	-	-	23
24	-	0.409	-	0.678	0.342	0.207	-	-	-	-	-	-	-	0.694	0.264	-	-	-	24
	1	2	3	4	5	6	7	8	9	10	11	12	13	14	15	16	17	18	

Longitudinal Grid Index. Increasing x >>>

(2B) Small Diameter Lug (2A)

Table A-3. Grid Element Equivalent Spherical Pit Radius (in).

d. Pit Severity

The final corrosion attribute used in this investigation was the pit severity which has been described in the Probabilistic Reliability chapter of the main body. It was not measured directly but derived from the combination of pit depth and pit volume. Pit severity was chosen for the development of a probability distribution because as a single attribute it combined two quantifiable attributes that directly effect the buckling strength of the drag strut. The computed grid pit severity values are shown in Table A-4 below.

Radial Grid Index. Increasing Angle About x-axis From x-z Plane. >>>

(1B) Large Diameter Lug (1A)

	1	2	3	4	5	6	7	8	9	10	11	12	13	14	15	16	17	18	
1	-	0.5	0.6	25.9	13.7	1.0	-	-	-	-	-	-	-	-	-	-	-	-	1
2	-	-	2.9	25.4	13.4	22.0	1.8	-	-	-	-	-	-	0.2	-	-	0.2	0.4	2
3	-	0.5	0.5	15.4	18.3	8.8	4.6	3.9	1.0	-	-	-	0.7	0.2	-	-	-	-	3
4	0.5	0.6	0.5	17.5	22.0	20.1	-	-	-	-	-	-	0.3	0.2	0.3	0.3	0.2	-	4
5	-	1.0	1.2	14.6	18.3	0.6	0.2	-	-	-	-	-	-	0.9	0.3	0.3	0.3	0.4	5
6	0.2	1.5	-	12.2	14.3	5.9	-	-	-	-	-	-	0.2	0.4	-	0.2	-	0.4	6
7	0.4	0.4	-	4.3	5.6	0.7	-	-	-	-	-	0.2	0.2	-	-	-	-	-	7
8	-	0.4	0.2	0.3	-	0.4	-	-	-	-	0.7	0.6	0.9	-	-	-	-	-	8
9	-	-	-	-	-	-	-	-	-	-	-	0.6	0.2	-	-	-	-	-	9
10	-	-	-	-	-	-	-	-	-	-	-	-	-	-	-	-	-	-	10
	1	2	3	4	5	6	7	8	9	10	11	12	13	14	15	16	17	18	
11	-	-	-	-	-	-	-	2.7	-	-	-	-	-	-	-	-	-	-	11
12	-	-	2.0	2.4	3.1	2.2	2.0	2.4	0.9	2.4	1.5	-	-	-	-	-	7.3	4.9	12
13	-	3.3	5.1	4.4	3.3	5.4	2.4	2.0	1.8	7.3	4.4	3.4	2.7	2.4	3.7	8.5	30.9	19.5	13
14	-	4.3	9.3	3.8	6.0	11.0	4.0	2.7	2.4	5.9	5.9	4.7	8.3	17.5	14.0	8.1	14.6	5.9	14
15	5.1	6.3	10.3	11.0	9.5	19.6	2.4	2.0	1.1	3.7	6.0	6.3	20.1	35.9	22.0	17.5	4.9	4.6	15
16	2.7	11.7	11.0	17.9	16.2	8.8	2.4	0.6	-	2.0	1.5	2.0	50.0	58.6	36.6	18.3	3.7	-	16
17	3.7	8.3	8.3	16.8	13.9	12.1	2.4	0.3	-	1.5	-	2.7	43.9	90.4	62.4	10.3	4.9	-	17
18	3.7	2.0	2.0	7.3	12.8	1.7	-	-	-	-	-	-	8.3	70.5	61.9	11.0	2.4	-	18
19	-	3.3	6.6	10.7	9.8	0.6	-	-	0.2	-	-	-	3.7	17.4	16.8	5.1	-	-	19
20	2.4	3.7	-	2.9	4.6	-	-	-	-	-	-	-	1.5	9.2	7.7	3.7	-	-	20
21	-	4.8	1.3	9.4	10.3	-	-	-	-	-	-	-	-	9.3	4.3	2.0	-	-	21
22	1.5	3.1	-	12.1	8.2	4.4	-	-	-	-	-	-	-	3.7	4.0	-	-	-	22
23	1.5	0.9	-	9.8	5.9	3.1	-	-	-	-	-	-	-	6.1	4.8	-	-	-	23
24	-	2.2	-	3.7	5.2	3.1	-	-	-	-	-	-	-	4.8	2.7	-	-	-	24
	1	2	3	4	5	6	7	8	9	10	11	12	13	14	15	16	17	18	

Longitudinal Grid Index. Increasing x >>>

(2B) Small Diameter Lug (2A)

Table A-4. Grid Element Pit Severity (x 10^{-6} in^4)

APPENDIX B. EQUIVALENT SPHERICAL PIT JUSTIFICATION

4. GENERAL CORROSION PROCESS

The high strength steel used in the drag strut is very susceptible to corrosion as evidenced by its position next to aluminum and magnesium on the Galvanic Series for Seawater, which is a widely used ranking or approximation of how metals behave in a corrosive environment. Because the metal is in a highly refined form, it is inherently unstable and is continually trying to revert to its natural mineral state. Unlike some other naturally self-protecting materials such as copper, corroding steel forms a loose, porous, and non-adhering oxide that tends to flake off and expose fresh metal to the corrosive environment. [Ref 8] This flaking process within the drag strut is shown in Figure A-4.

5. NUCLEATION SITES

The corrosive environment is established when moist air is forced into the strut during the numerous decompression and compression cycles of flight operations. It appears from observation of the sample strut that the moisture collects or beads up into droplets in certain areas, either on the top or bottom of the cylindrical portion. This is a naturally occurring phenomenon relating to surface energy that can be observed on the hood of a car after a rain. These droplets form localized corrosive cells, or nucleation sites, in which the corrosion initially propagates at the same rate in all directions, forming small spherical pits. The propagation rate; however is influenced by the molecular characteristics at any one site, which accounts for the rough, irregular boundaries of the corrosion sites. When several nucleation sites are adjacent, the pits eventually grow together, causing sharp boundaries between pits. These boundaries have higher potential and therefore corrode at a higher rate. Because the boundaries between pits corrode faster than the outside edges, the many small spherical pits grow together into one big pit. Also, because of the higher propagation rate at the sharp boundaries, the slope at the edge of the pits becomes more shallow than at the initial nucleation sites. Figure B-1shows an idealization of the process described above, which is the justification for the equivalent spherical pits used in modeling as describe in Appendix A.

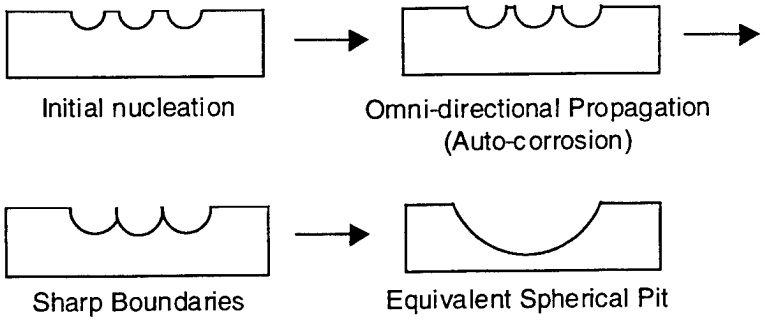

Figure B-1. Corrosion Propagation Idealization.

APPENDIX C. DRAG STRUT MODELING PROCEDURE

1. AutoCAD PROCEDURES.

a. Engineering Drawing.

The engineering drawing used to manufacture the strut was closely examined and annotated with all of the information that would be necessary input for constructing a CAD drawing. This included the center coordinates for all chamfer radii or other machining processes. All coordinates were referenced to the manufacturer's origin which was the center of the 0.562 inch diameter hole on the large lug end of the strut. The x-axis was selected to run down the longitudinal centerline. The y-axis was selected so that the centerline of the 0.562 inch diameter hole would be perpendicular to the x-y plane with the large lug end of the strut on the left. The coordinate system has been superimposed on the engineering drawing as shown in Figure C-1.

b. X-Y Plane Cross Section.

The cross section made by cutting the strut through the center with the x-y coordinate plane was drawn in AutoCAD using a series of line segments, arcs and circles. Only the upper portion of the cross section was drawn as if the strut were cut by the x-z coordinate plane. These lines were then trimmed as appropriate to form smooth intersections as indicated in the engineering drawing. The result was one closed line that described the exterior profile, the interior profile of the cylindrical portion, and the maximum radius of the large and small lug ends. The individual line segments that made up this closed line was then joined together into one continuous polyline. This polyline was then revolved 360 degrees about the x-axis to form a solid cylinder with hollow center and lug ends.

c. Virtual Machining and Trimming Process.

The machining process was simulated by constructing solid primitives (blocks, cylinders, and spheres) and locating them relative to the solid cylinder from above so that when subtracted from the drawing the required solid geometry would remain. In some cases the coordinate system had to be tilted first in order to properly align the primitives

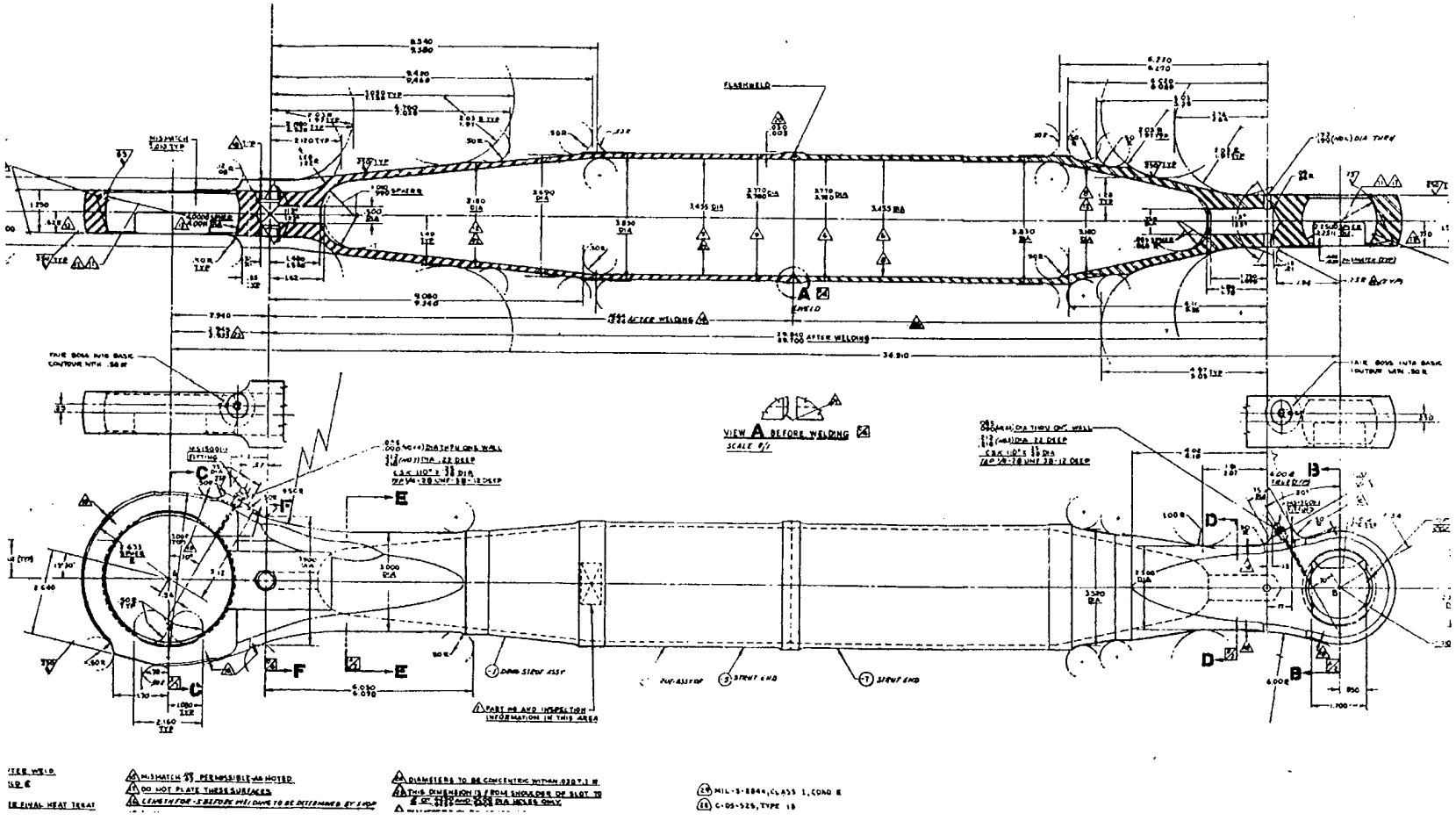

Figure C-1. Technical Drawing 901676, Drag Strut Assembly, Lower Main Landing Gear [Ref 3].

prior to subtraction. The result of this process was a virtual strut geometry that matched the real strut as described in Appendix A. Some of the protrusions on the lug ends of the strut were not modeled as they would only serve to increase the complexity of the model without contributing to the analysis. It was expected that the mass properties of the model would then be slightly less in magnitude than the real strut. The mass properties data computed directly by AutoCAD is shown below.

```
P-3C LOWER DRAG STRUT AutoCAD MODEL (strut_01.dwg)  05/21/98

Mass Property Computations with origin at 0.562" diameter hole
 ---------------   SOLIDS    ----------------

Mass:                    95.0449
Volume:                  95.0449
Bounding box:         X: -5.5750  --  33.6800
                      Y: -2.6350  --  2.6350
                      Z: -2.6350  --  2.6350
Centroid:             X: 13.4858
                      Y: -0.0013
                      Z: 0.0000
Moments of inertia:   X: 210.3237
                      Y: 31099.6935
                      Z: 31153.4474
Products of inertia: XY: -0.2087
                     YZ: 0.0024
                     ZX: -0.0021
Radii of gyration:    X: 1.4876
                      Y: 18.0890
                      Z: 18.1046
Principal moments and X-Y-Z directions about centroid:
                      I: 210.3234 along [1.0000 0.0001 0.0000]
                      J: 13814.0552 along [-0.0001 1.0000 0.0000]
                      K: 13867.8088 along [0.0000 0.0000 1.0000]


Mass Property Computations with origin at Centroid
 ---------------   SOLIDS    ----------------

Mass:                    95.1037
Volume:                  95.1037
Bounding box:         X: -19.0533  --  20.2017
                      Y: -2.6337  --  2.6363
                      Z: -2.6350  --  2.6350
Centroid:             X: 0.0000
                      Y: 0.0000
                      Z: 0.0000
Moments of inertia:   X: 210.3651
                      Y: 13822.8298
```

```
                        Z: 13876.5692
Products of inertia: XY: 1.4484
                     YZ: -0.0007
                     ZX: 0.0260
Radii of gyration:    X: 1.4873
                      Y: 12.0559
                      Z: 12.0793
Principal moments and X-Y-Z directions about centroid:
                      I: 210.3649 along [1.0000 0.0001 0.0000]
                      J: 13822.8299 along [-0.0001 1.0000 0.0000]
                      K: 13876.5692 along [0.0000 0.0000 1.0000]
```

The mass and moments of inertia presented above are in terms of volume and have units of in^3 and in^5 respectively. They had to be converted to the values presented in Appendix A by applying the material density for AISI 4340 steel which is 0.2836 lbm per in^3.

d. Eccentricity Representation

The manufactured drag strut can have a certain amount of eccentricity as a result of the flash weld process. The engineering drawing allows for as much as 0.045 inches mismatch in the diameters of the two cylindrical sections following welding and heat treatment. The AutoCAD model was sliced by a y-z plane at the center of the flash weld and the right half was displaced 0.0318 inches in both the positive y and z directions. The two halves were then joined together again into one 3D solid. This resulted in a total of 0.045 inches of offset causing an internal moment in the strut when loaded axially.

e. Corrosion Pitting Representation.

The pitting measured during the procedures outlined in Appendix A was included in the AutoCAD model as follows. The process involved creating spherical primitives at specific locations within the strut and then subtracting those spheres which left a spherical pit. The spheres were located according to the data presented in Table C-1 which is the pit center radial distance in each of the grid elements. The left most column in the table shows the longitudinal position and the top row shows the angular position around the cylinder for each grid element center. First, the AutoCAD work plane was rotated about the x-axis according to the angular position for a column of data. Then, a sphere was created, centered at the longitudinal position in the x direction and the radial

distance in the y direction. The radius of the sphere was set according to the data in Table A-3 which is the equivalent spherical pit radius for each grid. Then this sphere was subtracted from the strut, leaving the spherical pit. An example of the pitting is shown in Figure C-2.

Radial Position (deg). Increasing Angle About x-axis From x-z Plane. >>>

Longitudinal Position (in). Increasing x >>>	(1B) 10	30	50	70	90	110	130	150	170	Large Diameter Lug 190	210	230	250	270	290	310	330	(1A) 350	
10.425	-	1.494	1.540	1.216	1.465	1.126	-	-	-	-	-	-	-	-	-	-	-	-	1
10.925	-	-	1.511	1.503	1.207	0.867	1.152	-	-	-	-	-	-	0.517	-	-	0.517	1.192	2
11.425	-	1.430	1.430	1.213	1.372	1.260	1.306	1.435	1.126	-	-	-	1.575	0.517	-	-	-	-	3
11.925	1.430	1.540	1.430	1.221	1.489	1.141	-	-	-	-	-	-	0.954	0.517	0.954	0.954	0.517	-	4
12.425	-	1.126	1.346	1.159	1.372	0.177	0.517	-	-	-	-	-	-	0.940	0.954	0.954	0.954	1.192	5
12.925	0.517	1.466	-	1.256	0.961	0.657	-	-	-	-	-	-	0.517	1.336	-	0.517	-	1.192	6
13.425	1.192	1.336	-	1.242	0.932	0.653	-	-	-	-	-	0.517	0.517	-	-	-	-	-	7
13.925	-	1.336	0.517	0.954	-	1.192	-	-	-	-	0.653	0.177	0.940	-	-	-	-	-	8
14.425	-	-	-	-	-	-	-	-	-	-	-	0.177	0.517	-	-	-	-	-	9
14.925	-	-	-	-	-	-	-	-	-	-	-	-	-	-	-	-	-	-	10
	1	2	3	4	5	6	7	8	9	10	11	12	13	14	15	16	17	18	
16.250	-	-	-	-	-	-	-	1.479	-	-	-	-	-	-	-	-	-	-	11
16.750	-	-	0.519	0.216	0.763	0.775	1.254	1.392	0.940	0.958	0.823	-	-	-	-	-	0.387	0.181	12
17.250	-	0.295	1.143	0.927	0.295	0.451	0.958	1.254	1.152	1.047	0.927	0.933	1.093	0.216	0.569	0.746	0.936	0.964	13
17.750	-	0.375	1.134	0.055	1.044	0.702	0.772	1.093	0.958	0.657	0.657	0.612	1.202	1.221	1.376	0.252	0.357	0.657	14
18.250	1.143	0.817	0.548	0.702	0.357	1.229	0.958	1.254	1.254	0.569	1.044	0.817	1.141	1.226	0.867	1.221	0.181	1.306	15
18.750	0.535	1.474	1.140	1.125	0.987	1.260	0.958	0.177	-	0.519	0.823	0.519	1.524	1.180	0.999	1.013	0.569	-	16
19.250	0.569	1.202	1.202	1.303	1.095	1.381	1.392	0.954	-	0.823	-	1.479	1.536	1.229	1.082	0.242	0.181	-	17
19.750	1.062	0.519	1.254	1.269	1.597	0.147	-	-	-	-	-	-	1.202	1.228	1.291	0.702	0.216	-	18
20.250	-	0.295	1.380	1.422	1.353	0.177	-	-	0.517	-	-	-	1.062	0.934	1.303	0.792	-	-	19
20.750	0.958	0.569	-	1.196	1.525	-	-	-	-	-	-	-	0.823	0.875	0.845	1.062	-	-	20
21.250	-	1.047	0.543	1.462	1.508	-	-	-	-	-	-	-	-	1.310	0.375	0.519	-	-	21
21.750	0.823	0.763	-	1.381	0.961	1.500	-	-	-	-	-	-	-	0.569	0.772	-	-	-	22
22.250	0.823	0.940	-	1.353	0.657	1.538	-	-	-	-	-	-	-	1.499	1.047	-	-	-	23
22.750	-	1.331	-	1.062	1.403	1.538	-	-	-	-	-	-	-	1.047	1.479	-	-	-	24
	1	2	3	4	5	6	7	8	9	10	11	12	13	14	15	16	17	18	
					(2B)					Small Diameter Lug								(2A)	

Table C-1. Grid Element Pit Center Radial Distance From Strut Center (in).

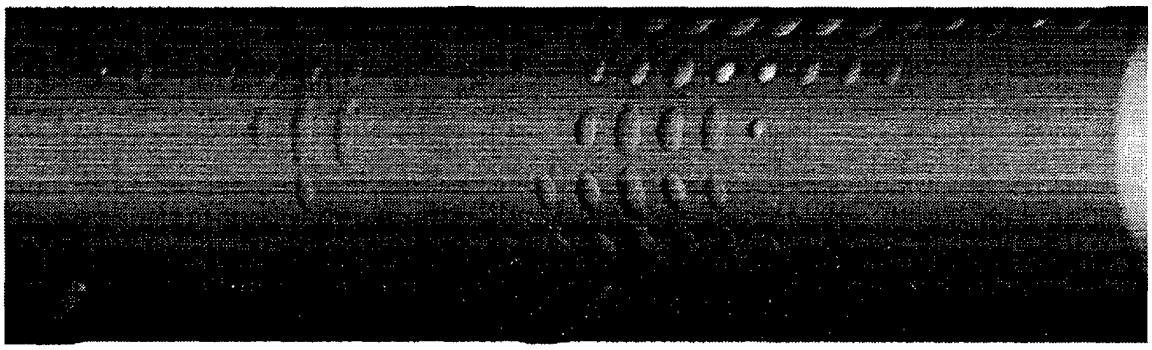

Figure C-2. Strut Model Including Grid Element Spherical Pitting.

f. ACIS File Export

Following the modeling procedures, the AutoCAD 3D solid geometry was exported into an ACIS file to facilitate use by NASTRAN.

2. NASTRAN FOR WINDOWS PROCEDURES

The following is a list of the abbreviated steps accomplished in NASTRAN for Windows for each of the 34 configurations of drag struts that were modeled.

a. File / Import / Geometry...

1) Change to directory where ACIS file resides
2) Solid Model Read Options: OK (Accept default)
3) NASTRAN loads solid geometry with all curves and surfaces that define the geometry.

b. Model / Material...

1) ID: 1
2) Load: AISI 4340 Steel
3) Mass Density: change to 0.2836 (So that mass properties come out in correct units.)
4) OK / Cancel

c. Model / Property...

1) ID: 1
2) Title: Drag Strut Solid
3) Elem/Property Type: Volume Elements / Solid / OK
4) Material: AISI 4340 Steel (From list)
5) OK / Cancel

d. Geometry / Curve / From Surface / Slice...

1) Solid ID: 1
2) Methods: Coordinate System Plane – yz plane (x = -2.94)
3) Repeat for x = 31.97

(This step is necessary to add two curves to the solid geometry that will allow future selection of nodes on a surface for applying boundary conditions.)

e. File / Save As... (Save the geometry alone using a descriptive filename)

f. Mesh / Geometry / Solid...

1) Element Size: 0.420 (Or as appropriate for model complexity to stay under 5,000 node limit)
2) OK

3) Property: 1..Drag Strut Solid
4) Midside Nodes: OFF (Unless model complexity allows)
5) OK
6) If 5,000 node limit exceeded then Tools / Undo (CTRL + z) to remove the nodes and try again with larger maximum element size.

g. Modify / Renumber...

1) Node... / Select All / X coordinate order
2) Element... /Select All / X coordinate order

h. Model / Node... (Add nodes for bearings)

1) Coordinates: (-2.94, 0, 0)
2) Coordinates: (31.97, 0.0318, 0.0318)

i. Model / Element...

1) Type: Rigid / OK
2) Node (Independent)
3) Select bearing center node
4) Nodes (Dependent)
5) Method: On Surface
6) Select bearing surfaces / OK
7) OK
8) Repeat for other bearing

j. Model / Load / Nodal...

1) Name: Tension or Compression
2) Select large bearing node
3) Force / Vector / Specify...
4) Change to snap to node (Right mouse click)
5) Select start node
6) Select finish node
7) Magnitude: 1
8) OK

k. Model / Constraint / Nodal...

1) Name: Bearing
2) Select bearing node
3) Select DOF (Large: 2/3/4, Small: 1/2/3)
4) OK
5) Repeat for other bearing

l. Customize View

1) View Quick Options (CTRL + q)
2) All Entities Off
3) Check: Elements, Loads, Constraints

4) Done
5) View / Select (F5)
6) Full Hidden Line – OK

m. File Rebuild / Yes / Yes

n. File / Save As... (Save the finite elements in new descriptive name)

o. File / Save As...

1) Save copy in F:\Scratch*.mod (This forces all scratch files created during analysis to be placed in the Scratch directory.)

p. File / Analyze...

1) Type: Buckling (or Static for Tension)
2) Output Types: Displacements and Stresses
3) Eigenvalues: 2 or 3 (Buckling only)
4) OK
5) OK to save file... Yes

3. MAKING PITS WITH NASTRAN

a. View / Options... (F6)

1) Tools and View Style
2) Workplane and Rulers
3) Check Draw Entity
4) OK (Turns the workplane and rulers on so one can verify that the workplane is properly aligned for future coordinate references.)

b. View / Rotate... (F8) – As required so that the required x-y plane will be in the plane of the screen with the z-axis coming out of the screen.

c. Tools / Workplane / Select Plane...

1) Method... / Align to View

d. View / Rotate... (F8) – As required to allow 3D verification of solid primitive direction and placement. Trimetric works well.)

e. Geometry / Solid / Primitives / Sphere...

1) Radius: 0.318 (or as desired)
2) Coordinates: (Example for 0.318 radius sphere)
Mode 1: 15.083, -1.5690
Mode 2: 16.008, -1.5372
Mode 3: 5.598, -1.1580
3) Remove (Negative direction)

4) OK

(Nodes for modes 1 & 3 direct. Node 2 adjust y for offset.)

4. MAKING HOLES WITH NASTRAN

a. Perform steps 3 a through 3 d above.

b. Geometry / Solid / Activate...

1) Select the desired solid (1..Drag Strut Solid)

c. Geometry / Solid / Primitives...

1) Select Cylinder
2) Material: Remove
3) Direction: As required to orient the solid properly (Use the reference arrow as a guide.)
4) Origin: Enter x and y coordinates
5) Primitive: Select Cylinder
6) Radius: as desired
7) Height: as desired (will build from the x-y plane in the z direction that is selected as shown with the arrow.)
8) OK

APPENDIX D. ALUMINUM TUBE BUCKLING TESTS

1. TUBE BUCKLING TESTS

The absolute accuracy of the FE buckling solutions for the drag struts could not be validated by an actual buckling test with a real strut; however buckling tests were performed on straight hollow aluminum tubes with fixed-end conditions. A NASTRAN model was created that matched the geometry, material, and loading boundary conditions of the tubes. Because both the tube and strut models matched their real counterparts, the buckling analysis results could be compared. A search was made of available stock to match the critical buckling characteristics of the strut as closely as possible. The first characteristic was the diameter to thickness ratio, which for the drag strut is 23.59. The closest match was found at 19.23 with seamless Al 2024-T3 tubes that were 1.25 inches in diameter with a wall thickness of 0.065 inches. Next, the length of the tubes was chosen to match the slenderness ratio of the drag strut (effective length divided by cross section radius of gyration). This value was 27.28 for the drag strut which resulted in a test length of 11.5 inches for the tubes. Additional tube lengths of 8, 10, 12, 13, and 23 inches were tested to provide further resolution on the FE results. Finite element solutions were computed for all of the test lengths, including additional lengths of 30 and 45 inches to investigate buckling behavior in the purely elastic region of the material. The test and analysis results are presented in Table D-1 and Figures D-1and D-2 below. In addition to the test and FE solutions, the results from the appropriate form of the classical Euler column buckling equation for fixed end conditions are provided. The form of the Euler equation is [Ref. 9]:

$$P_E = \frac{4\pi EI}{L^2} \qquad \text{(D1)}$$

The results show that the FEA buckling load values and the Euler equation values were significantly higher than the tested values, as expected; however the compressive yield values matched very closely. The buckling mode shape, half sinusoidal wave, matched what was observed which lends credence to the boundary conditions included in

Aluminum Tube Buckling Test Data - 8/13/98 & 9/3/98						
Sample	Length (in)	Buckling Load, P_{cr} (lbs)	Mean P_{cr} (lbs)	Euler Load, P_E (lbs)	FEA Load, P_{fe} (lbs)	Al 2024-T3 Modulus, E = 1.0700E+07 Tube Moment of Inertia, I = 0.0426 Notes
1	8.0	14200	14200	281173	118010	9/3/98 Yield Load = 10,000 lbs (NASTRAN 10,042 lbs)
2	10.0	13450	13475	179951	114742	
3	10.0	13500				
4	11.5	13150				
5	11.5	13050				
6	11.5	13000	12933	136068	108932	
7	11.5	12900				
8	11.5	12850				Added dial gage to detect lateral deflection
9	11.5	12650				Began strain control process in final stage of loading
10	12.0	12750	12750	124966	101734	
11	12.0	12750				
12	13.0	12300	12400	106480	89187	
13	13.0	12500				
14	23.0	10400	10400	34017	32094	9/3/98
15	30.0			19995	19333	
16	45.0			8886	8765	P_{cr} determined from extrapolation

Table D-1. Aluminum Tube Buckling Test Data and Analysis Results.

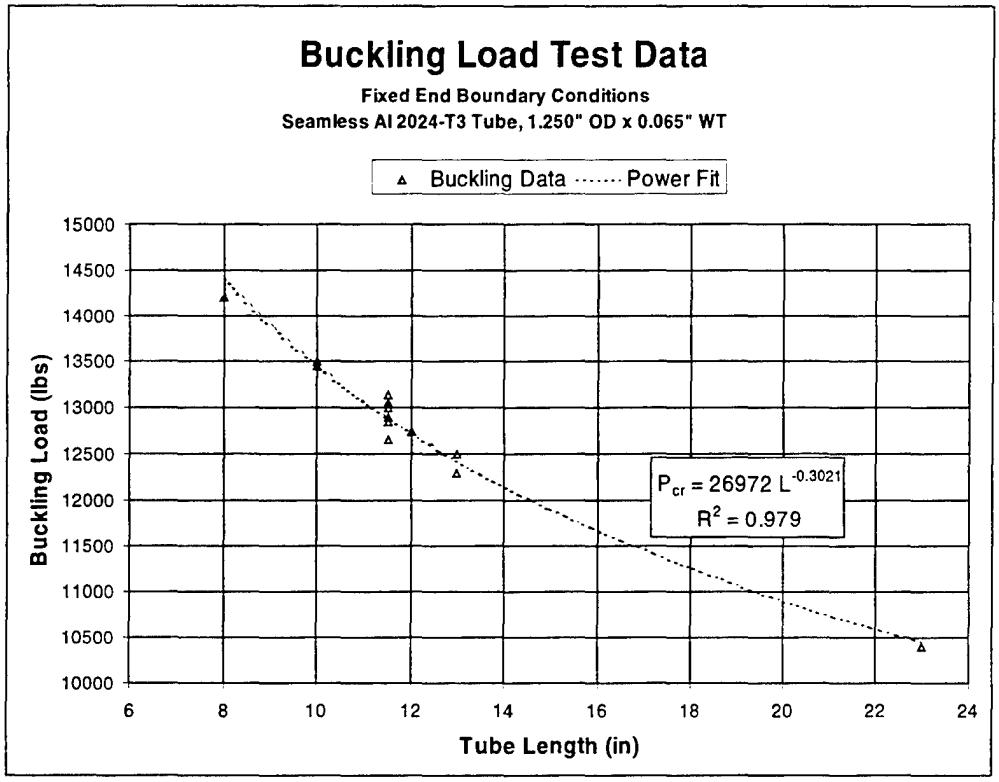

Figure D-1. Aluminum Tube Buckling Test Results.

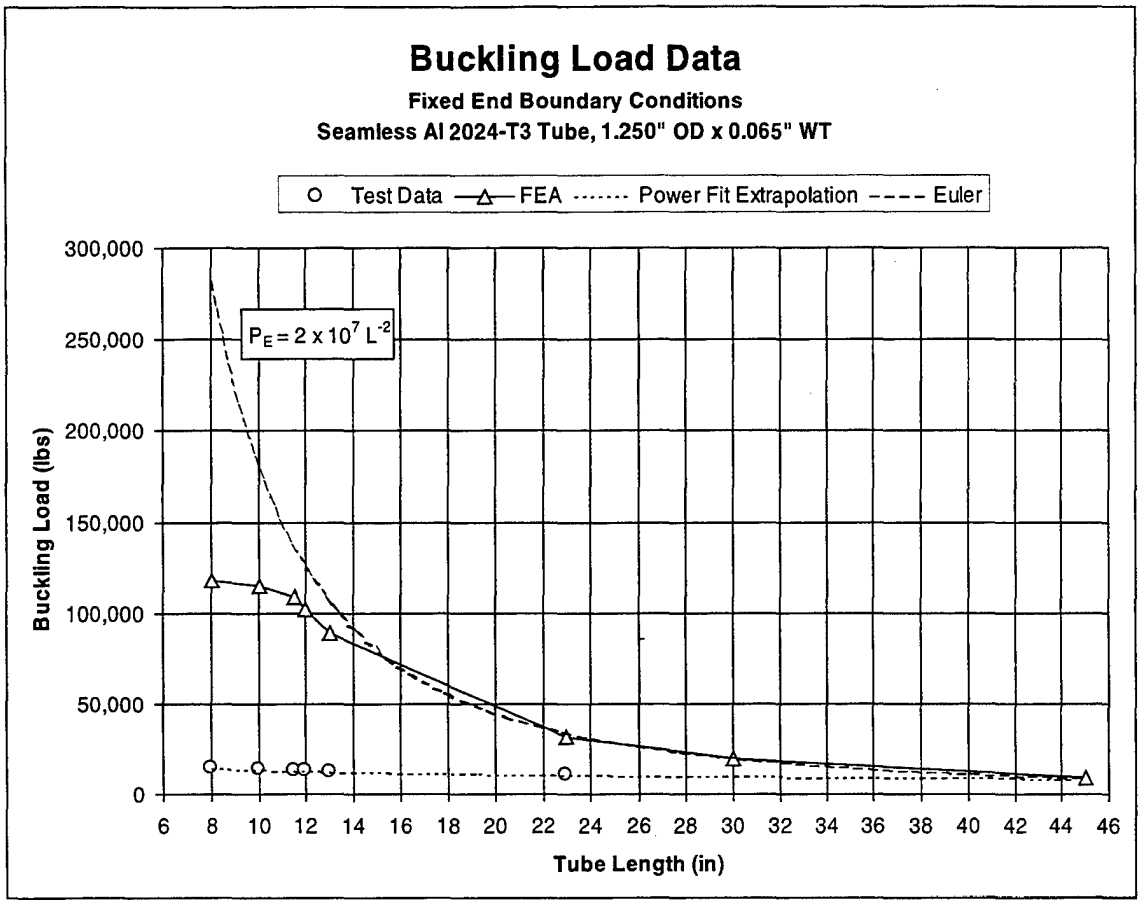

Figure D-2. Test, Analysis, and Euler Buckling Data Combined.

the model. The FE solution indicated that the first yielding, on an individual element level, would occur around 10,000 pounds. The 8 inch test length was selected specifically to determine the yield load. The specimen was short enough to fit into a digital caliper with a resolution of ± 0.0005 inches. The length prior to test was measured at 8.0550 inches. The tube was placed under compressive loads in 500 pound increments with length measurements between each step until a permanent change in length was observed. This occurred at a load of 10,000 pounds when the measured length changed to 8.0545 inches.

2. INTERPRETATION OF RESULTS

The most important result of the tube buckling tests was observation of the convergence upon accurate FEA solutions when the physical geometry caused buckling within the linear elastic region of the material. This should be self evident because the FEA solution was performed under the linear-elastic assumption. However, this testing revealed the order of magnitude of divergence and monotonic relationship between the solution and the real test when the linear-elastic assumption was violated. The results indicate a predictable trend in solution values as the geometry of the tube was changed. The conclusion was that the same assumption could be made about the drag strut as physical geometry was changed due to corrosive pitting. In addition, the results indicate that high confidence could be placed in the determination that buckling of the drag strut could only occur following plastic deformation. Therefore, because the FEA solutions provided a very accurate prediction of yield load, if one could assure that a corroded strut would not yield under an operational load, then the same assurance could guarantee that it would not buckle under that load.

INITIAL DISTRIBUTION LIST

1. Defense Technical Information Center 2
   8725 John J. Kingman Rd., Suite 0944
   Ft. Belvoir, VA 22060-6218

2. Dudley Knox Library 2
   Naval Postgraduate School
   411 Dyer Rd.
   Monterey, CA 93943-5101

3. Commander, Naval Air Systems Command (AIR-4.1.1.3) 1
   Attn: Mr. Nam D. Phan
   47123 Buse Rd., Bldg. 2272
   Patuxent River, MD 20670

4. Commander, Naval Air Systems Command (PMA-290) 1
   Attn: P-3 Class Desk Officer
   47123 Buse Rd., Bldg. 2272, Rm. 146
   Patuxent River, MD 20670

5. Prof. Gerald H. Lindsey, Code AA/Li 1
   Chairman, Department of Aeronautics and Astronautics
   Naval Postgraduate School
   Monterey, CA 93943-5000

6. Prof. Edward M. Wu, Code AA/Wu 3
   Department of Aeronautics and Astronautics
   Naval Postgraduate School
   Monterey, CA 93943-5000

7. Commanding Officer 1
   Attn: Mr. Chuck Lipscomb, Code 4.3.3
   Naval Aviation Depot
   NAS Jacksonville, FL 32212-0016

8. CAPT Harold E. Rice, USN (Ret.) 1
   1625 Lehigh Parkway, North
   Allentown, PA 18103

9. Mr. Claude A. Hodges 1
   1926 Brandon Ave., SW
   Roanoke, VA 24015

10. Commander, Naval Air Warfare Center, Weapons Division 1
Attn: CDR(S) Christopher W. Rice, Code 00C000D
1 Administration Circle
China Lake, CA 93555-6100